

# Lattice and Orientational Defects Mediate Collective Transport of Confluent Cells

Jiushi Zhang<sup>1</sup>, Chung Wing Chan<sup>1</sup>, Bo Li<sup>2,3</sup>, and Rui Zhang<sup>1\*</sup>

<sup>1</sup>*Department of Physics, Hong Kong University of Science and Technology, Clear Water Bay, Kowloon, Hong Kong SAR*

<sup>2</sup>*Institute of Biomechanics and Medical Engineering, Applied Mechanics Laboratory,  
Department of Engineering Mechanics, Tsinghua University, Beijing 100084, PR China*

<sup>3</sup>*Mechano-X Institute, Department of Engineering Mechanics, Tsinghua University, Beijing 100084, PR China*

(Dated: June 14, 2025)

Confluent tissues are a type of foam-like biological active matter. There is a recent interest in using active nematic liquid crystal framework to understand confluent cells, where topological (orientational) defects are believed to play a crucial role. However, how to reconcile the physical picture of lattice defects in Voronoi polygons with that of orientational defects in the nematic field—particularly in the context of cellular transport—remains elusive. Here, we employ the Active Vertex model to investigate the physics of lattice and orientational defects in the dynamics of confluent cells. We find a spatio-orientational correlation between lattice defects and  $+1/2$  defects, unveiling a correspondence between the two physical perspectives. Next, we simulate the behavior of a dragged cell within a hexagonal-lattice tissue. Our results reveal that while the drag coefficient is anisotropic, the threshold drag force to mobilize the cell is isotropic, indicating the presence of a caging energy barrier. We further analyze the defect pattern in the wake of the dragged cell or cells. Remarkably, we discover that dragging two neighboring cells along the least-drag direction can substantially minimize the destruction of the lattice structure during cell transport. We find that this is due to the cooperative and periodic self-healing of the lattice defects. Taken together, our work sheds new light on the topological structure of confluent cells during their collective motion, advancing our physical understanding of cellular transport in processes such as wound healing, cancer cell metastasis, and other physiological events.

## I. INTRODUCTION

Confluent cells represent a unique type of soft material, which comprises closely packed, active, and deformable biological cells [1, 2]. Over the past decade, there has been a growing multidisciplinary interest in studying these confluent cell systems [3–5]. From a physicist’s perspective, confluent cells can be considered as a form of active matter [6], where the collective dynamics of self-propelled cells can lead to the emergence of various spatiotemporal patterns [7–12]. This perspective has provided valuable insights into many biological processes, including embryonic development [13], wound healing [13–15], cancer progression [13, 16, 17], and cell fate dynamics [18]. Moreover, in the field of bioengineering, a deeper understanding of and a better control over the structural and rheological properties of confluent cells can greatly enhance their applications in tissue engineering, regeneration, and transplantation [19].

A characteristic mechanical property of confluent cells is their motility-mediated liquid–solid transition [20–22]. The melting (solid-to-liquid) transition is also termed epithelial–mesenchymal transition, during which the rheological properties of the cells vary markedly, such that cells can migrate collectively with motility [23, 24]. The reverse process is also studied as the glass transition [20, 25, 26]. Theory and experiment have demonstrated that the glass transition in these systems is influenced by cellular activity, surface tension, and cell–cell interactions [25, 27–32]. For example, confluent cells typically exhibit fluid-like behavior when intercellular adhesion outweighs intracellular contraction, particularly when combined with elevated cell motil-

ity. [25, 27, 33]. Another recent work points out that intracellular nuclear mechanics—such as nuclear jamming—can also impact the glass transition of confluent cells [34].

The anisotropy and deformability of confluent cells are also important for their structures and dynamics. For example, confluent cells have been recently examined using an active liquid crystal (LC) framework [8, 9, 35, 36]. Specifically, a monolayer of confluent cells can be regarded as a two-dimensional (2D) nematic LC, in which neighboring anisotropic cells tend to align with each other. 2D nematic is characterized by the presence of topological defects, including comet-like  $+1/2$  defects and trefoil-like  $-1/2$  defects [37]. Interestingly, these orientational defects have been observed in different biological systems [8, 38–41]. Due to their singularity, these defects can induce mechanical stresses and flows in confluent cells [42, 43]. Orientational defects also have biological consequences, as they can influence the collective dynamics of cells during tissue morphogenesis [36, 44, 45] and regulate cell fate, including apoptosis and extrusion [18, 46]. Note that many tissues consisting of contractile cells can exhibit extensile behavior, which is attributed to the influence of the polar fluctuating forces [40, 42, 43, 47] as well as adhesion proteins [48].

Because confluent cells can be represented by polygons, their foam-like structure should also be correlated with their collective mechanics. Cells with more than and less than 6 neighbors are categorized into positive (+L) and negative (−L) lattice defects, respectively. These lattice defects are not just structural irregularities but may hold biological significance, potentially playing a critical role in the embryo development, functioning, and morphogenesis of epithelial tissues [34, 49–52]. When near the glass transition point, the hexatic order of the “foam” can be enhanced [53–56]. However, how to reconcile the two structural characterizations, namely, the nematic order and the lattice structure, remains

\* ruizhang@ust.hk

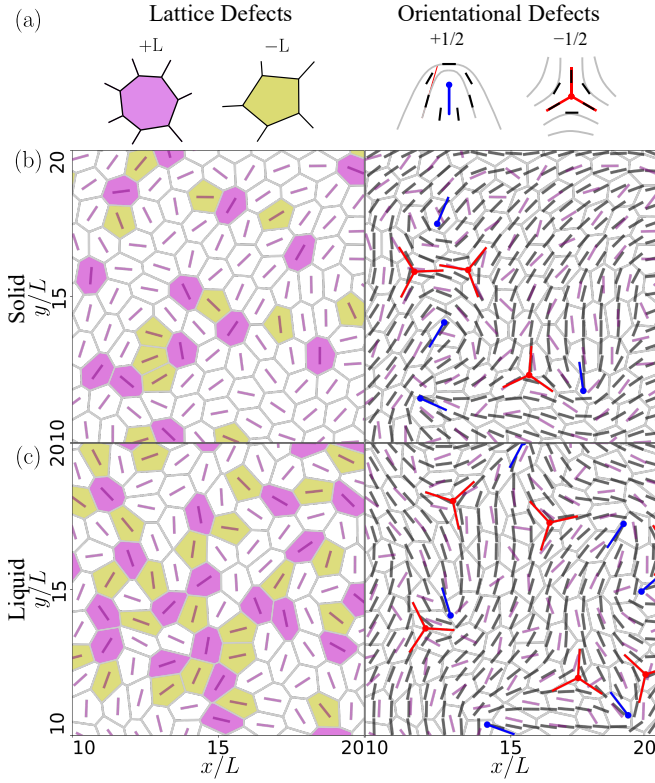


FIG. 1. Defects in the AVM model. (a) Representative pictures of lattice defects and orientational defects. (b) A snapshot of the system (left) and the corresponding director field (right) in the solid state with  $\bar{v}_0 = 0.3$  and  $p_0 = 3.55$ . (c) A snapshot of the system (left) and the corresponding director field (right) in the liquid state with  $\bar{v}_0 = 0.3$  and  $p_0 = 3.85$ . +L- and -L-defect cells are marked purple and yellow, respectively, and +1/2 and -1/2 defects are marked by blue lines and red trefoils, respectively.

an open question. A recent work has shown that pentagons tend to appear in the center of the +1 defect [57]. Nevertheless, a systematic comparison of the two frameworks remains at large to date. Moreover, during cell proliferation, transport, and rearrangement, how different types of defects mediate the structural evolution of confluent tissues is rarely studied.

Therefore, here we use simulation to address the above-mentioned open questions. Specifically, we adopt the Active Vertex Model (AVM) to study the structure of confluent cells under self-propulsion and external driving forces. We analyze two types of topological defects in the model confluent tissues, namely orientational defects and lattice defects. We uncover a spatial correlation between orientational defects and lattice defects, which is enhanced in the solid state. Moreover, our *in silico* cell-drag experiment on a hexagonal lattice shows that confluent cells have to overcome an isotropic energy barrier to migrate, despite the anisotropy of the background lattice. Interestingly, we further find that dragging two neighboring cells can eliminate most lattice defects in the wake of their trajectories. Finally, we discuss the underlying mechanism of this defect auto-healing process.

## II. ACTIVE VERTEX MODEL

To investigate the physical interactions among confluent cells, various 2D computational models have been developed to effectively describe phenomena such as glass transition, cell migration, and cell mechanics [4, 5]. These models include Self-Propelled Voronoi (SPV) model [25, 58], Active Vertex Model (AVM) [27], multiphase field model [30, 59, 60], Active Tension Network model [61], mesoscopic model [42], and cellular Potts model [26, 55, 62]. Among them, we choose AVM to investigate the structure of confluent tissues subjected to the active motions of cells [12, 63], as it offers a minimum model with detailed representations of the cellular structures and well-defined physical boundaries. Additionally, its computational efficiency makes it suitable for large-scale simulations, which are achieved by retaining the essential interactions necessary to capture the many-body interactions among cells.

We construct a 2D network of cell vertices to represent a confluent cellular system of  $N = 900$  cells undergoing internal stresses in a  $30 \times 30$  box with periodic boundary conditions in both directions (SM Movie 1). To incorporate cell motility in the AVM [27], each cell is self-propelled at a constant speed  $v_0$  along a direction that is free to rotate. The self-propulsion direction of the cell  $i$ , represented by an angle  $\theta_i$ , follows a Wiener process with a persistence time scale  $\tau_p$ , which characterizes the cell's tendency to maintain its directional motion. The equations of motion for the angle  $\theta_i$  of the self-propulsion direction of the cell  $i$  and the position vector  $\mathbf{r}_\mu$  of the vertex  $\mu$  are, respectively [64],

$$\frac{d\theta_i}{dt} = \sqrt{2D_r}\xi(t), \quad (1)$$

$$\frac{d\mathbf{r}_\mu}{dt} = \frac{1}{\zeta}\mathbf{F}_\mu + v_0 \sum_{i \in C_\mu} \hat{\mathbf{n}}_i, \quad (2)$$

where  $D_r = 1/\tau_p$  sets the persistence time of the cell,  $\xi(t)$  represents a normalized white noise term with zero mean and delta-correlation satisfying  $\langle \xi(t)\xi(t') \rangle = \delta(t - t')$  [65],  $\zeta$  is the friction coefficient of the cell,  $\mathbf{F}_\mu$  is the force acting on vertex  $\mu$ , and  $C_\mu$  is the set of cell indices that contain vertex  $\mu$ . The unit vector  $\hat{\mathbf{n}}_i = (\cos \theta_i, \sin \theta_i)$  represents the self-propulsion direction of cell  $i$ . The free energy of the system is given by [33]

$$E_{\text{AVM}} = \sum_{i=1}^N \left[ \frac{K}{2}(A_i - A_0)^2 + \frac{\Gamma}{2}P_i^2 \right] + \Lambda \sum_{(\mu,\nu)} l_{\mu\nu}, \quad (3)$$

where  $K$ ,  $\Gamma$ , and  $\Lambda$  are elasticity, contraction, and adhesion modulus, respectively,  $A_0$  is the target (preferred) cell area,  $A_i$  and  $P_i$  are the area and perimeter of cell  $i$ , respectively, and  $l_{\mu\nu}$  is the edge length if two vertices  $\mu$  and  $\nu$  are connected. The force acting on a vertex  $\mu$  can be decomposed into three contributions [27, 29, 64, 66]:

$$\mathbf{F}_\mu = \mathbf{F}_\mu^{\text{elas}} + \mathbf{F}_\mu^{\text{con}} + \mathbf{F}_\mu^{\text{ad}},$$

where

$$\mathbf{F}^{\text{elas}} = \sum_{i \in C_\mu} \frac{K}{2} (A_i - A_0) \begin{bmatrix} 0 & 1 \\ -1 & 0 \end{bmatrix} \cdot (\bar{l}^{\text{CW}} - \bar{l}^{\text{CCW}}), \quad (4)$$

$$\mathbf{F}^{\text{con}} = \sum_{i \in C_\mu} \Gamma P_i (\hat{l}^{\text{CW}} + \hat{l}^{\text{CCW}}), \quad (5)$$

$$\mathbf{F}^{\text{ad}} = \sum_{i \in C_\mu} \Lambda (\hat{l}^{\text{CW}} + \hat{l}^{\text{CCW}}). \quad (6)$$

In the above equations,  $\bar{l}^{\text{CW}}$  and  $\bar{l}^{\text{CCW}}$  are line vectors of the edges that point clockwise and counter-clockwise from the vertex  $\mu$ , respectively. We also introduce a dimensionless shape parameter  $p_0$  by comparing the energy Eq. (3) with another form of the free energy [33]:

$$E_{\text{AVM}'} = \sum_{i=1}^N \left[ \frac{K}{2} (A_i - A_0)^2 + \frac{\Gamma}{2} (P_i - P_0)^2 \right], \quad (7)$$

$$p_0 = \frac{P_0}{\sqrt{A_0}} = -\frac{\Lambda}{\Gamma \sqrt{A_0}}, \quad (8)$$

where  $p_0$  sets the target shape of the cells via the ratio between the adhesion modulus  $\Lambda$  and the contraction modulus  $\Gamma$ .  $p_i = \frac{P_i}{\sqrt{A_i}}$  is the shape parameter for cell  $i$ , which indicates its degree of elongation. The simulation is based on the Euler algorithm. We identify the two types of defects and perform calculations over the statistics of these defects (Fig. 1).

We express all quantities in terms of fundamental dimensions. The length unit  $L$  is chosen such that the target area of a cell is  $A_0 = 1$ , which gives rise to a lattice constant of the perfect hexagonal lattice in the simulation to be  $a = \sqrt{\frac{2A_0}{\sqrt{3}}} \approx 1.075L$ . For conciseness, the unit  $L$  may be omitted in the following discussions. By choosing an arbitrary time unit  $\tau_0$ , the velocity unit is given by  $L/\tau_0$ . The dimensionless activity parameter  $\bar{v}_0 \equiv v_0 \tau_0 / L$  will be adopted in what follows. In our simulation,  $\bar{v}_0$  is varied within  $0 < \bar{v}_0 < 1$ , while the shape parameter  $p_0$  is constrained to  $3.3 < p_0 < 4$ .

T1 transition is an important process for confluent cells to rearrange their neighbors and locomote while generating collective cell migration [67]. During a T1 transition, four cells in a quadrilateral arrangement reorganize [68]: cells initially in contact by an edge will lose the edge and detach, while the other two cells become in contact by gaining an edge. When the length of an edge falls below a critical threshold of  $\delta l = 0.2$ , the minimum-energy configuration from three possible arrangements will be adopted in the next time step: the two T1 configurations (from switching vertices clockwise or counterclockwise) and the unchanged configuration.

### III. NEMATIC ORDER ANALYSIS

To investigate the behavior of the orientational defects in our AVM model, we calculate the elongation direction for cell  $i$  by computing the eigenvector corresponding to the largest

eigenvalue of the shape tensor  $\mathbf{f}_i$  as defined as:

$$\mathbf{f}_i = \frac{1}{\sum_j l_{ij}} \sum_j l_{ij} \mathbf{n}_{ij} \otimes \mathbf{n}_{ij}, \quad (9)$$

where  $\mathbf{n}_{ij} \otimes \mathbf{n}_{ij}$  represents the dyadic product of the unit vector  $\mathbf{n}_{ij}$  for an edge between cell  $i$  and its neighbor cell  $j$ , and  $\mathbf{f}_i$  is a  $2 \times 2$  tensor describing the shape of the cell  $i$ . We further transform the discrete orientational fields of cells into a director field on a regular grid through interpolation (Appendix A). For the nematic order analysis, we introduce a symmetric, traceless  $\mathbf{Q}$ -tensor defined as [43]:

$$\mathbf{Q} = \begin{bmatrix} \cos 2\psi_i & \sin 2\psi_i \\ \sin 2\psi_i & -\cos 2\psi_i \end{bmatrix}, \quad (10)$$

where angle  $\psi_i$  represents the elongation direction for cell  $i$ . We obtain a continuous and ordered  $\mathbf{Q}$ -tensor field by interpolating the components of the director,  $\cos 2\psi_i$  and  $\sin 2\psi_i$ . The director field can be acquired by calculating the eigenvectors of the  $\mathbf{Q}$ -tensor. To identify the location of orientational defects, we calculate the winding number and use the surrounding directors to determine the orientations of the defects (Appendix B). This physics-based approach provides results consistent with our recently developed AI-based defect detection method [69]. More details about the director field extraction and defect detection are provided in Appendix A.

## IV. RESULTS AND DISCUSSION

### A. Lattice defect statistics

The number of neighboring cells for a cell, namely cell neighbor (coordination) number  $z$ , is an important quantity to characterize the structure of the tissue [49, 70]. For a 2D confluent tissue, the ground state configuration is a hexagonal lattice with  $z \equiv 6$  for every cell. Cells with greater or fewer neighbors are called lattice defects (or defect cells). Here, we measure the ensemble average of the cell area  $\bar{A} = \langle \frac{1}{N} \sum_{i=1}^N A_i \rangle$  and the shape parameter  $\bar{p} = \langle \frac{1}{N} \sum_{i=1}^N p_i \rangle$  at steady state as functions of different parameters for the two types of defect cells and the hexagonal cells in Fig. 2. We find that compared to the reference hexagonal cells with  $z = 6$ , +L-defect cells with  $z > 6$  are larger and rounder, while -L-defect cells with  $z < 6$  are smaller and more elongated (Fig. 2, Appendix Fig. 8). In other words, cells with fewer neighbors will favor a more anisotropic shape. This can be understood by the fact that the statistical variation of the intercellular forces, which dictates the shape of the cell of interest, depends on the number of neighboring cells—a smaller number of neighboring cells implies a larger variation, which can lead to a more anisotropic cell shape. The fact that +L-defect cells are larger in area  $\bar{A}$  is because their shape, with more edges, is closer to a circle.

Although  $\bar{v}_0$  and  $p_0$  play a similar role in dictating the phase of the confluent cells as demonstrated in the phase diagram of AVM model [25, 56], their impacts on the different types of

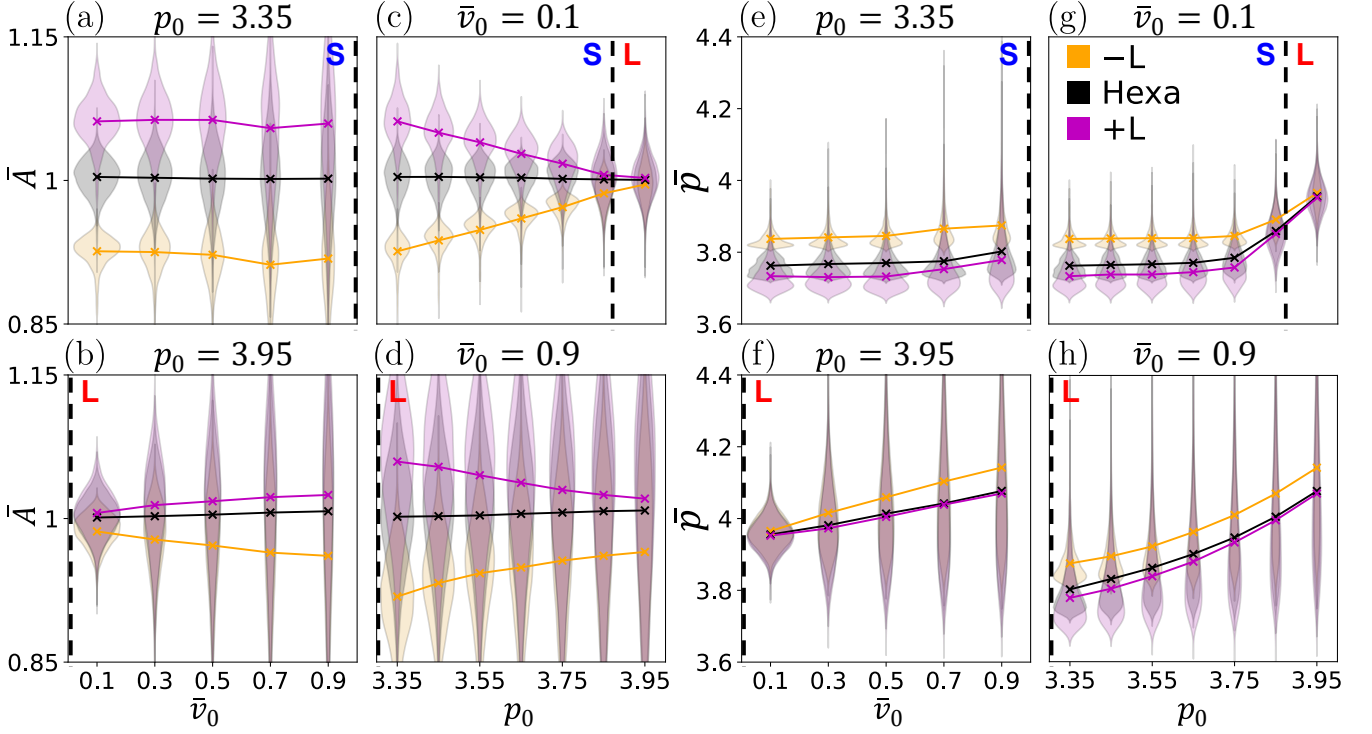


FIG. 2. Statistics of different types of cells. (a–d) Violin plots of the average cell area  $\bar{A}$  for +L-defect, –L-defect, and hexagonal cells. (e–h) Violin plots of the average shape-parameter  $\bar{p}$  for +L-defect, –L-defect, and hexagonal cells. The dashed lines mark the transition point between the solid and liquid phase.

cells are different. By varying the activity parameter  $\bar{v}_0$  with a fixed shape parameter  $p_0$ , we find that the difference in the average area  $\bar{A}$  between the three types of cells is insensitive to  $\bar{v}_0$  in the solid state (Fig. 2(a)), but it increases as  $\bar{v}_0$  increases in the liquid state (Fig. 2(b)). This implies that the effect of activity in the solid state is insensitive to the magnitude of the activity, as cells are trapped in their local positions and their activity acts similar to thermal noise. In the liquid state, however, cells with different  $z$  exhibit different mobilities, as cells with less (more) neighbors can squeeze more (less) at higher activity, leading to smaller (larger)  $\bar{A}$  (Fig. 2(b)). If we fix  $\bar{v}_0$  but vary  $p_0$ , the trend is very different: the difference in  $\bar{A}$  among the three types of cells diminishes as  $p_0$  increases, and this trend is independent of the phase of the system (Fig. 2(c, d)). A higher  $p_0$  can promote deformations and rearrangement of all types of cells, which can homogenize them, giving rise to less differences in  $\bar{A}$ .

The behavior of the average cell-shape parameter  $\bar{p}$  is similar to that of  $\bar{A}$  (Fig. 2(e–h)). But there is a general trend in  $\bar{p}$ : as the system moves towards a more liquid-like state,  $\bar{p}$  among all three types of cells will increase, because cells become more elongated and also more homogeneous in the more liquid-like state. Because the total area of all cells is a conserved quantity, there is no general trend for the change in the  $\bar{A}$  plot (Fig. 2(a–d)).

Our analyses also reveal that the hexatic phase emerges at the onset of the solid-liquid transition, characterized by a peak in the hexatic order and a corresponding minimum in lattice

defect density (Appendix Fig. 9) [71]. Below the transition, limited cell motility prevents defect annihilation and hexagonal ordering, while above the transition, increased activity disrupts the spatial order, leading to a rise in defect density (Appendix C, Fig. 9, 10, and 11). This behavior is consistent with previous theoretical and numerical studies on the hexatic phase [53, 55, 56, 71, 72]. However, the density of  $\pm 1/2$  defects does not exhibit any critical behavior around the transition point. This indicates that the nematic order is not sensitive to the hexatic order of confluent cells.

Analysis of the statistics of the lifetimes of L defects reveals that their distribution follows an exponential function. We find that the half-life of L defects, namely  $t_{1/2}$ , decreases toward zero as the system moves toward the liquid state, at which defect proliferation and annihilation events occur more frequently (Appendix D, Fig. 12 and 13).

## B. Self-propulsion of cells and +1/2 defects

To understand the collective dynamics of confluent cells, we next focus on the statistics of self-propelled cells and defects. We introduce two angles,  $\phi_c$  and  $\phi_{+1/2}$ , to represent the velocity angle of a cell and a +1/2 defect, respectively (Fig. 3(a)). As shown in Fig. 3(b), cells prefer to move along their elongation axis, despite the inherent randomness in their self-propulsion directions. Since cell velocity is determined by a combination of its activity and cell–cell interaction

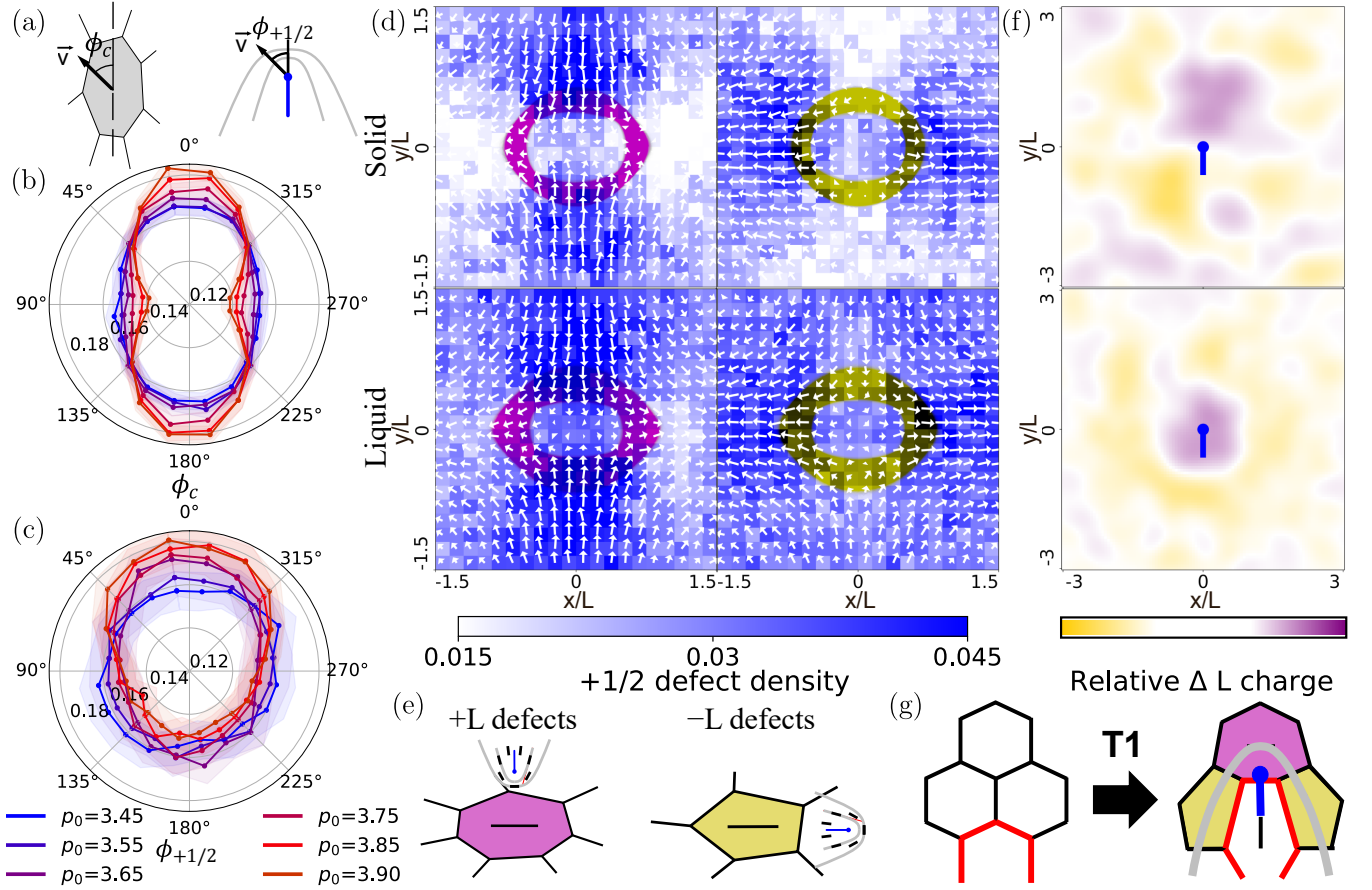


FIG. 3. Statistics of cells, lattice defects, and orientational defects. (a) Schematic definitions of two angles. Left: angle between a cell's velocity vector and its long axis,  $\phi_c$ ; right: angle between a  $+1/2$  defect's velocity vector and its orientation direction,  $\phi_{+1/2}$ . (b) Rose-plot of the histogram of  $\phi_c$  at  $\bar{v}_0 = 0.3$ . (c) Rose-plot of the histogram of  $\phi_{+1/2}$  at  $\bar{v}_0 = 0.3$ . Different colored curves are for different  $p_0$ . The liquid–solid transition point is  $p_0 \approx 3.7$ . (d) Heatmap of the distribution of  $+1/2$  defects around an average  $+L$ -defect cell (purple) and an average  $-L$ -defect cell (yellow) in the solid (upper) and liquid (lower) state. The white arrows indicate the average orientation of the  $+1/2$  defects at that point. (e) Schematic diagrams showing how  $+1/2$  defects tend to orient and spatially distribute around  $\pm L$  defects. (f) The distribution of  $\pm L$  defects around an average  $+1/2$  defect in the solid ( $\bar{v}_0 = 0.3$ ,  $p_0 = 3.55$ ) and liquid ( $\bar{v}_0 = 0.3$ ,  $p_0 = 3.85$ ) state. (g) A schematic explanation of the spatio-orientational correlation between L defects and  $+1/2$  defects by looking at how a cell invades an otherwise hexagonal lattice.

forces, this directional bias suggests that cells experience reduced resistance from neighboring cells along their elongation axis compared to the transverse direction. This effect becomes particularly pronounced deep in the liquid state of the system, where cells are, on average, more elongated. In cell monolayers, there is a robust correlation between the direction of the intercellular stress and the instantaneous cell velocity, which is known as plithotaxis [73, 74]. This anisotropic stress field also dictates cellular morphology, inducing local orientational order in cell elongation. Therefore, intercellular stress provides the mechanistic link connecting the preferred direction of cell velocity and the axis of cell elongation.

A similar analysis on  $+1/2$  defects shows that they tend to propel along their head direction, and this trend is pronounced in the liquid state with high  $p_0$  (Fig. 3(c)). This implies that confluent cells in the AVM model can be mapped to an extensile active LC—this result is consistent with a recent theoretical prediction [43]. But our work points out that this extensile

character is weakened in the solid state with low  $p_0$ . This  $p_0$  dependence of the defect behavior echoes another recent experimental finding that cell–cell adhesion is responsible for the extensile behavior of the tissue [40]. We further show that  $+1/2$  defects in the liquid state exhibit enhanced extensile character when they age (Appendix E, Fig. 14). This is because newly generated defects have to overcome the attractive force by the oppositely charged defects and thereby exhibit weak extensile behavior; as they age, they unbind and their self-propulsion becomes more directional.

### C. Correlation between lattice and orientational defects

Next, we investigate the statistical correlation between  $+1/2$  defects and L defects. By analyzing the probability distribution of  $+1/2$  defects around an average  $+L$ - or  $-L$ -defect cell in either solid or liquid state, we observe different corre-

lation patterns (Fig. 3(d)). In the solid state,  $+1/2$  defects are predominantly located on the two sides of a  $+L$ -defect cell, oriented towards the cell. In contrast, near a  $-L$ -defect cell in the solid state,  $+1/2$  defects are more likely to appear in the two end regions of the cell, facing outwards. In the liquid state, this spatio-orientational correlation is weakened due to frequent neighbor exchanges, which disrupt the lattice-defect patterns and weaken the correlation. This spatio-orientational correlation is also schematically shown in Fig. 3(e).

The correlation between the two types of defects can alternatively be characterized by the probability distribution of  $L$ -defect cells around an average  $+1/2$  defect (Fig. 3(f)). In the solid state,  $+L$ -defect cells are predominantly located in the head region of the  $+1/2$  defect (purple), while  $-L$ -defect cells are more likely to be found in the tail region (yellow) (Fig. 3(f)). In the liquid state, however,  $+L$ -defect cells are more frequently observed in the core regions of the  $+1/2$  defect.

These spatio-orientational correlation patterns can be qualitatively understood by an illustrative picture shown in Fig. 3(g). When a cell invades an otherwise hexagonal lattice, the cell immediately in front of the invading cell gains an additional neighbor and becomes elongated in the orthogonal direction due to the mechanical force exerted by the invader. Meanwhile, cells on the two sides of the invading cell, initially in contact, are now pushed apart, losing coordination number  $z$  and at the same time being stretched along the invasion direction. Therefore, this process induces the formation of a  $+1/2$  defect, with its head area occupied by  $+L$ -defect cells and tail area filled with  $-L$ -defect cells (Fig. 3(e)). This picture well rationalizes the observation that  $+1/2$  defects tend to stay on either side of  $+L$ -defects and face towards them, but prefer to stay near the end region of  $-L$ -defects and face backwards.

The above statistical findings are further supported by several confluent cell experiments [18, 40, 75] (Appendix F, Fig. 15). A recent study on nematic-hexatic correlations using a multiphase field model also produced very similar correlation statistics [60], further confirming that this spatio-orientational correlation is model independent.

## D. Dragging one cell

To investigate how cell migration impacts confluent tissues and to probe their rheology, we conduct cell-drag simulations. As shown in Fig. 4a, a cell is dragged by a constant external force  $F_d$  in a hexagonal lattice in the solid state at low activity ( $\bar{v}_0 = 0.1$ ,  $p_0 = 3.65$ ). The dimensionless force  $\bar{F}_d \equiv F_d/(\zeta V)$  is used in the subsequent discussion. To account for the six-fold symmetry of the lattice, the force is applied at various angles,  $\Psi_d$ , with respect to the  $x$ -axis, ranging from  $0^\circ$  to  $30^\circ$ .

When  $\bar{F}_d$  is below certain threshold  $\bar{F}_c \equiv F_c/(\zeta V)$ , the cell remains trapped near its initial position due to the blocking of the surrounding cells. Interestingly,  $\bar{F}_c$  is independent of the force angle  $\Psi_d$ , indicating an isotropic free energy barrier that the cell must overcome to escape from. When  $\bar{F}_d \geq \bar{F}_c$ , the

cell will move persistently along a specific direction (Fig. 4, Appendix Fig. 16). Interestingly, the hexatic state exhibits the same threshold force as the solid phase,  $\bar{F}_c \simeq 4$ , while the liquid state shows a smaller threshold force,  $\bar{F}_c \simeq 3$ . Compared to the solid and hexatic state, cells in the liquid state can move around and change neighbors more easily. Therefore, the caging energy characterized by  $\bar{F}_c$  is smaller in the liquid state.

We further find that the mean velocity  $\bar{v}$  of the dragged cell subjected to a fixed  $\bar{F}_d$  is a function of the force angle  $\Psi_d$  (Fig. 4(b, c)). The cell moves fastest when  $\Psi_d = 0^\circ$ , at which it tends to travel along a “zigzag” tunnel between two horizontal layers of the hexagonal lattice (SM Movie 2). In contrast, the cell moves slowest when  $\Psi_d = 30^\circ$ . At this unfavorable force angle, the dragged cell cannot find a viable pathway without colliding with other cells. This drag-coefficient anisotropy vanishes in the liquid state (SM Movie 3).

During the continuous dragging, the cell experiences resistance due to cell-cell interactions (excluded-volume repulsion and adhesion). By tracking the trajectory of the dragged cell in all directions, we observe that the migration angle may deviate from the force angle  $\Psi_d$ , exhibiting a weak directional locking effect (Appendix Fig. 16). This occurs because cells experience the least drag along  $0^\circ$ , causing them to migrate towards this “locking” direction.

When  $\Psi_d = 30^\circ$ , the dragged cell experiences the highest resistance. Due to the symmetry of the lattice, it migrates at  $30^\circ$  on average. Its trajectory exhibits strong fluctuations in the orthogonal direction, indicating that the cell can diffuse perpendicular to the force direction. Our measurements of its diffusion along the perpendicular direction reveal a super-diffusive behavior, that is, the mean square displacement along that direction scales as  $\sim t^\alpha$ , where  $\alpha \simeq 1.15$  (Appendix Fig. 17).

By monitoring the velocity of the dragged cell, we further observe that it exhibits persistent stick-slip motion when  $\bar{F}_d > \bar{F}_c$ , which can be characterized by intermittent trapping within cages (evidenced by speed dropping to zero; see Appendix Fig. 18). This stick-slip behavior persists over a wide range of conditions within the regular hexagonal lattice, contrasting with homogeneous tissues where the stick-slip behavior can transition into a more continuous motion when  $\bar{F}_d$  is well above  $\bar{F}_c$  [30]. The stick-slip motion mode breaks down at  $\Psi_d = 0^\circ$  in our simulation, at which the dragged cell moves with fluctuating but nonzero velocity, exhibiting continuous locomotion without the “stick” mode (Appendix Fig. 18). This can be understood by the fact that at this special force angle, the dragged cell can easily sneak through two horizontal layers of cells.

We also observe that the dragged cell tends to elongate into a  $+L$  defect (i.e., gaining neighbors), with its elongation direction parallel to its migration direction (Fig. 4(a)). Cells in its front tend to gain neighbors and are stretched in the orthogonal direction, occasionally forming  $+L$  defects. Therefore, a  $+1/2$  defect can be seen in front of the dragged cell (Fig. 4(a)). This simultaneous formation of  $+1/2$  and  $L$  defects can also be understood by the spatio-temporal correlation found in the steady state (Fig. 3). Interestingly, the illus-

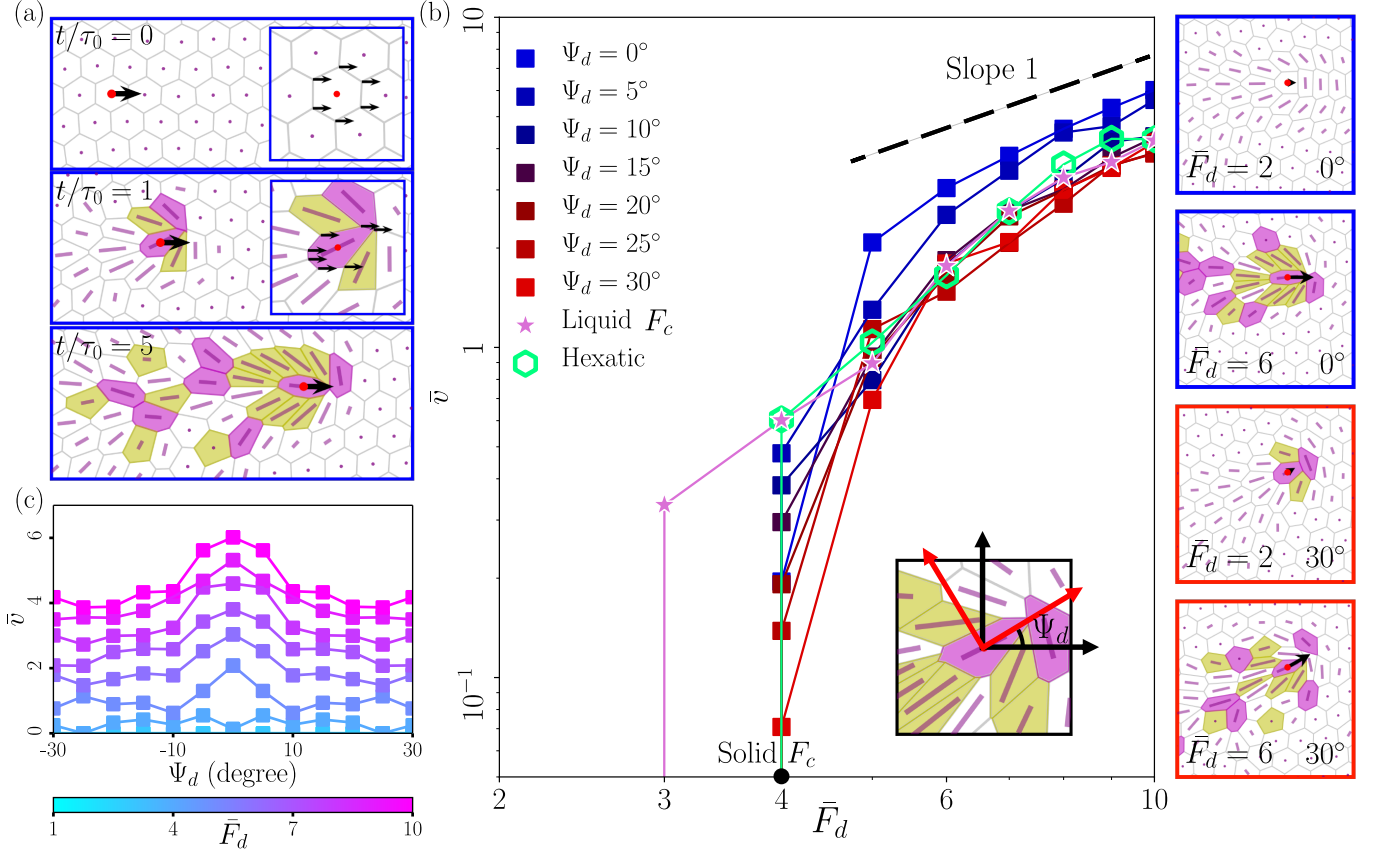


FIG. 4. Single-cell drag simulation. (a) Snapshots of the system when a cell is dragged with  $\bar{F}_d = 6$  and  $\Psi_d = 0^\circ$ . Insets: cell dragging is realized by applying additional forces to its vertices. (b) The velocity-force relation for the dragged cell at different force angles in the solid state ( $\bar{v}_0 = 0.1$  and  $p_0 = 3.65$ ), the hexatic state ( $\bar{v}_0 = 0.3$  and  $p_0 = 3.65$ ), and liquid state ( $\bar{v}_0 = 0.5$  and  $p_0 = 3.65$ ); right four panels: steady-state snapshots of the system for different parameter sets  $(\bar{F}_d, \Psi_d)$ . The threshold force for both the solid and hexatic state is  $F_c = 4$ . (c) The average velocity  $\bar{v}$  of the dragged cell plotted against force angle  $\Psi_d$  for different  $\bar{F}_d$ .

trative picture of a cell invading a hexagonal lattice can also be applied to here to understand the formation of defects around the dragged cell (Fig. 3(g)).

### E. Dragging two cells

During the dragging of a single cell, lattice defects are generated in the wake of its trajectory, and they do not spontaneously annihilate and restore the hexatic order; instead, they form a persistent trace of L defects that disrupt the hexagonal lattice structure (Appendix Fig. 19(a)). To look for the possibility of healing these wake defects, we have explored various cell-dragging scenarios, including dragging an additional cell over the wake region, back-and-forth dragging of a cell, and dragging two cells in various ways (Appendix G, Fig. 19, SM Movie 4). Among these, remarkably, we find that defect-healing can happen when two neighboring cells are dragged together along  $\Psi_d \simeq 0^\circ$  (SM Movie 5). As shown in Fig. 5, defect cells are only present around the initial and final locations of the two dragged cells.

We next analyze the lattice structure during the dragged

motion of two neighboring cells. As the two cells advance, we observe a group of lattice defects surrounding them and they form a compact cluster exhibiting a highly regular pattern, which we term them the “auto-healing packet” (Fig. 5(a)). As the packet advances with the two dragged cells, its Burgers vectors amount to zero, indicating the neutrality of lattice defects within this region (Fig. 5(a)). However, this packet contains five more cells than a perfect hexagonal lattice occupying the same region (Fig. 5(a)). Among these additional cells, two of them are the dragged cells, and one cell right behind them, namely the “follower cell”, is also transported together, exhibiting a large displacement vector (Fig. 5(a)). These three cells form the core of the packet (Fig. 5(b)). During the motion of the packet, two rows of cells will advance collectively and therefore contribute to the two additional cells in the packet (Fig. 5(a, b)). When the packet passes through an otherwise perfect lattice region, two local cells will advance by one lattice constant  $a$ , and all other cells will return to their initial locations (Fig. 5(b)).

Within the packet, two cells in front of the dragged cells tend to form +L defects, which we term them header cells. On the two sides of the three core cells, -L-defects appear

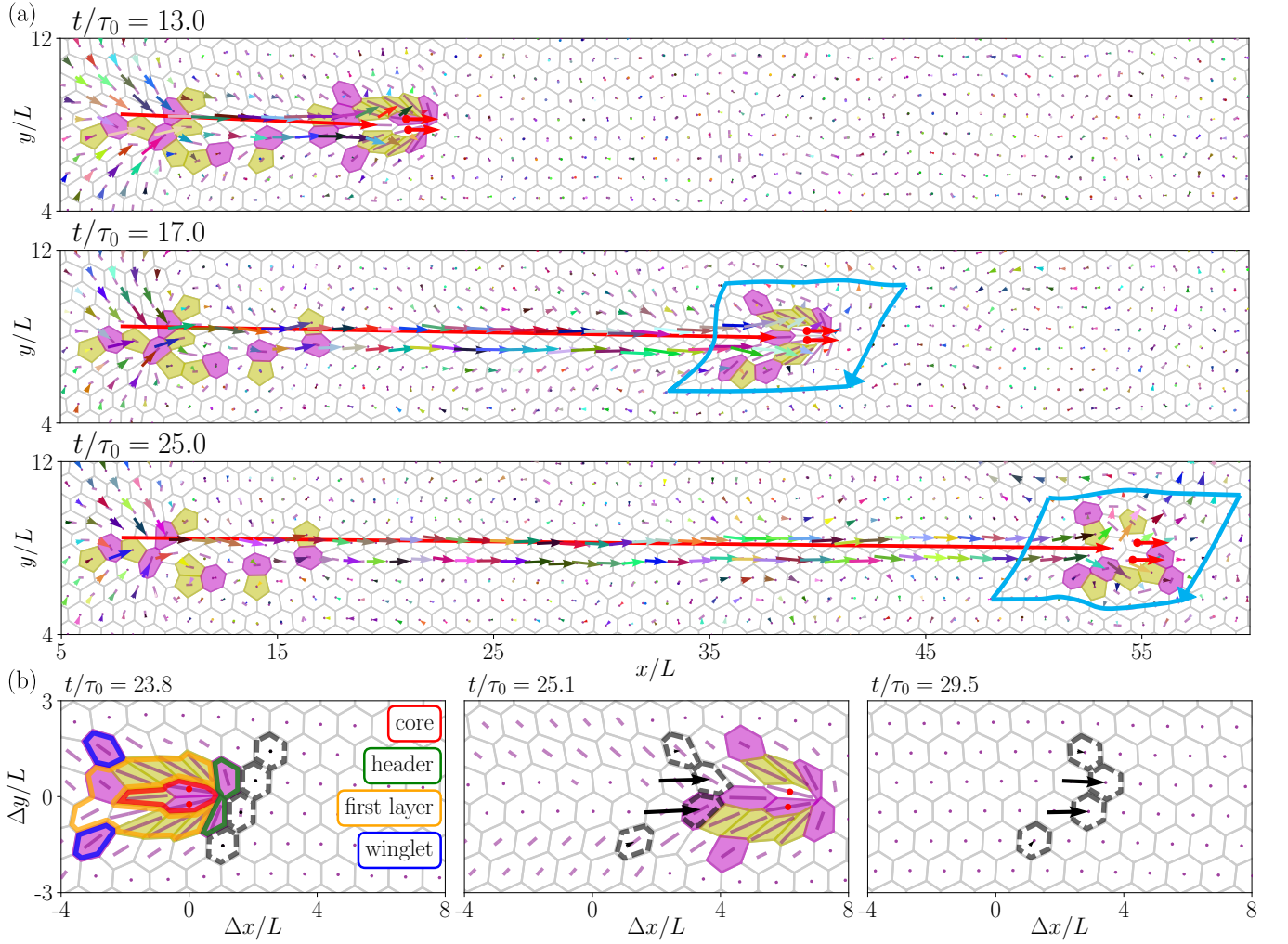


FIG. 5. Double-cell drag simulation. (a) Snapshots of dragging two neighboring cells at  $\Psi_d = 0^\circ$ ,  $\bar{F}_d = 6$ . The blue vectors are the Burger's vectors around a packet of the moving cells containing lattice defects. To clearly distinguish the displacement vector field of the cells, we use random colored arrows pointing from the initial position at  $t/\tau_0 = 10$  to the current position. (b) Snapshots of the packet undergoing auto-healing of lattice defects, along with the displacement vectors for black-outlined cells across different layers before and after the packet passes through.

and we call them the first-layer cells. These cells can also be seen in the single-cell drag simulation (Fig. 5(b)). To compensate for the topological charge of the packet,  $+L$  defects tend to form at the tail of the first-layer cells, with another two  $+L$ -defect cells located in the second (outer) layer, which we term winglet cells (Fig. 5(b), Appendix H, Fig. 20). As will be elaborated below, these charge-compensating defect cells change dynamically during the motion of the packet and mediate in the auto-healing of  $L$  defects in the wake region (Appendix Fig. 20).

We further analyze the temporal behavior of the system and find that the spectrum of the contraction and adhesion energy, defined as  $E_P = \sum_{i=1}^N \frac{\Gamma}{2} (P_i - P_0)^2$ , exhibits a pronounced peak at  $T_{f_1} = 2.5T_0$ , where  $T_0$  is the characteristic time scale for a dragged cell to advance by one lattice constant  $a$  (Fig. 6(a, b), Appendix I, Fig. 22). By examining the snapshots of the packet corresponding to the peak and valley

points of the  $E_P$  plot, we observe an interesting periodic-like behavior of the packet structure, in which the winglet cells play an important role. As the system evolves from a peak (valley) point to the next peak (valley) point, the two winglet cells located on the sides of the packet will advance by  $\sim 2a$  and  $\sim 3a$ , respectively (Fig. 6(c, e) and Fig. 6(d, f)); during the next period, however, the two cells will advance in an alternative manner, i.e., by  $\sim 3a$  and  $\sim 2a$ , respectively (Fig. 6(e, g) and Fig. 6(f, h)). Therefore, after two periods, the packet represented by the winglet cells will advance  $5a$ . This gives rise to the emerging period  $T_{f_1} = 2.5T_0$  for the advancing packet. During the motion of the packet, defect cells in the wake can auto-heal in a periodic manner while the winglet cells are advancing (Appendix H).

The nontrivial period of  $2.5T_0$  can also be found in the temporal behavior of other quantities (Appendix Fig. 22), such as the coordination number  $z$  of the follower cell (Appendix

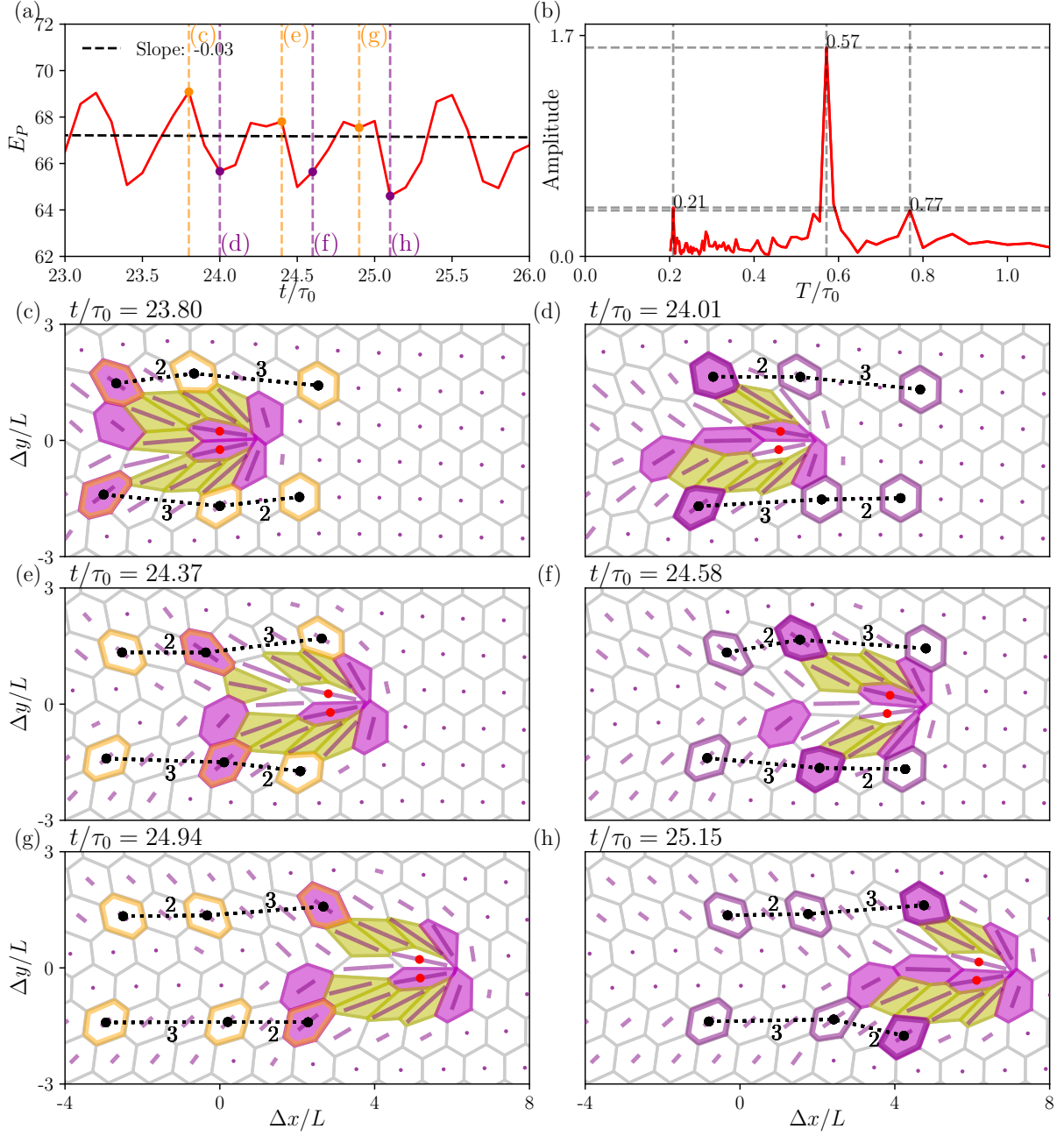


FIG. 6. Periodicity observed in the double-cell drag simulation. Temporal behavior (a) and the Fourier analysis (b) of the contraction and adhesion energy  $E_P$  at  $\bar{v}_0 = 0.01$  and  $p_0 = 3.65$ . Snapshots of the packet for peak points (c, e, g) and valley points (d, f, h) in the  $E_P$  plot. The positions of the winglet cells are highlighted with orange and purple outlines for the peak and the valley state, respectively.

Fig. 22(h)). Also note that this auto-healing behavior is robust against simulation parameters. Under variations of the background activity  $\bar{v}_0$ , force magnitude  $\bar{F}_d$ , and force angle  $\Psi_d$ , we can still observe a perfect lattice in the wake of the trajectories of the two dragged cells (Appendix Fig. 23).

## V. DISCUSSION

In this work, we have systematically investigated the correlation between orientational and lattice defects using the AVM model. A higher activity  $\bar{v}_0$  not only liquefies the system but also differentiates +L-, -L-defect, and hexagonal cells, promoting global fluctuations as well as collective cell migration. A larger shape parameter  $p_0$  also liquefies the confluent cells but homogenizes different types of cells.

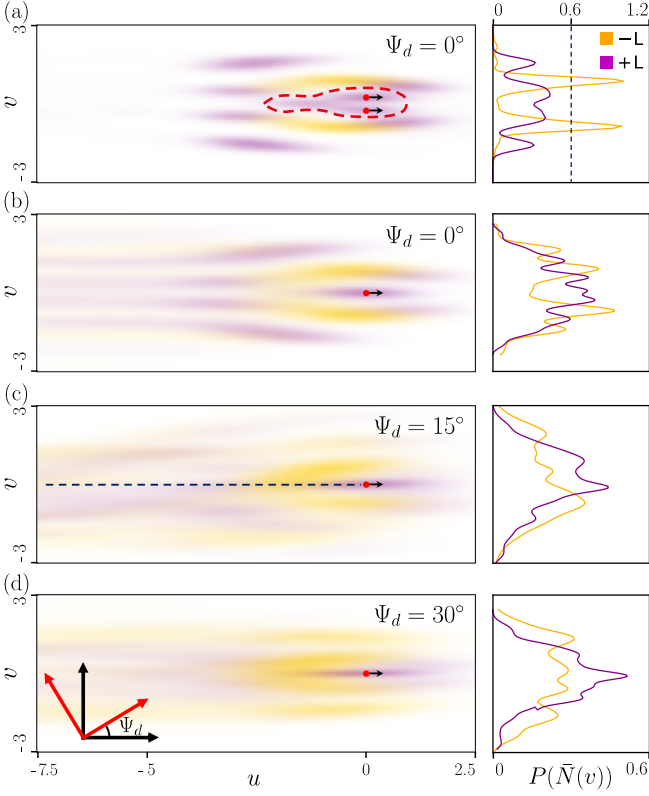


FIG. 7. Heat maps of the steady-state distribution of L defects in cell drag simulations. The coordinate system  $uv$  is chosen such that the  $u$ -axis is the force direction. +L and -L defects are colored purple and yellow, respectively. (a) Double-cell drag simulation. (b–d) single-cell drag simulation with  $\Psi_d = 0^\circ$  (b),  $15^\circ$  (c), and  $30^\circ$  (d). Right panels: the corresponding charge distribution  $P$  averaged over the  $u$ -axis as a function of the  $v$ -coordinate. In all the above cases,  $\bar{F}_d = 6$ .

We also demonstrate that the age and lifetime of topological defects contain important information about the structure and dynamics of confluent cells. For example, by tracking orientational defects in the system, we find that they exhibit stronger extensile character when they age, as they are more likely to unbind from their counterpart defects.

By probing the connection between cell-morphology dictated nematic order and cell-topology dictated lattice structures, we establish a spatio-orientational correlation between  $+1/2$  defects and L defects. Geometrical constraints imposed by lattice defects modulate the distribution of  $+1/2$  defects. The correspondence between the distribution of L defects and  $+1/2$  defects in confluent cells is also confirmed in published experiments as well as in other simulation models.

By simulating a cell dragged in a hexagonal lattice in the solid state, we generate advancing  $+1/2$  defects and observe the induction of surrounding L defects. The core of the advancing  $+1/2$  defect predominantly consists of +L defects, with the  $+1/2$  defects heading toward the +L defects and is trailed by -L defects, confirming the spatial correlation between these defect types. Additionally, we identify anisotropic migrations under the 6-fold symmetry where cells

experience the highest drag at  $\Psi_d = 30^\circ$ . There is a weak directional locking effect as cells tend to migrate at  $0^\circ$ , at which the dragged cell experiences the least drag by managing to locomote between two rows of cells.

The single-cell drag simulation can be interpreted as an active microrheology measurement, where the dragged cell functions as a driven probe requiring a critical force  $F_c$  to escape from its local cage. This critical force is quantitatively linked to the macroscopic yield stress of the system [76], and this is consistent with the yielding behavior observed in the microrheological analysis of solid-state confluent cells with low  $\bar{v}_0$  and  $p_0$  [29]. Beyond  $\bar{F}_c$ , the probe fluidizes its surrounding microenvironment, inducing a finite effective viscosity. The post-yielding force-velocity relationship exhibits a linear regime ( $\bar{F}_d > \bar{F}_c$ ), analogous to the microrheological response of a homogeneous viscoelastic medium [77]. By introducing the apparent viscosity as  $\eta_{\text{app}} \propto \frac{\bar{F}_d}{\bar{v}}$ , the system demonstrates a weak shear-thinning behavior above the critical force (Fig. 4).

We also perform double-cell drag simulation, in which we observe auto-healing of L defects in the wake of the dragged cells. This auto-healing phenomenon is accompanied by a periodic transformations of lattice defects contained in a compact packet. The auto-healing packet, with a vanishing Burgers vector, comprises five intruding cells: three in the core and two in the two first-layers. The free energy analysis shows that the adhesion and contraction energy  $E_P$  exhibits a periodic oscillation, with a nontrivial period of  $T_{f_1} = 2.5T_0$ . This periodicity reveals a “pedestrian”-like walking pattern of the packet, as the two winglet cells advance alternatively in “2+3” and “3+2” manner, during which wake defects are able to self-heal.

To understand the structure of wake defects and why double-cell drag can heal L defects, we compare the distribution of L defects around the dragged cell(s) for different cell-drag simulations. The L-defect heatmap in the double-cell drag simulation shows sharp spatial patterns, with the colored regions corresponding to the different types of cells in the packet (Fig. 7(a), Appendix Fig. 24(b)). In the single-cell drag scenarios, however, the L-defect heatmap is blur and shows long tails in the wake (Fig. 7(b–d)). The key difference between dragging two cells and dragging one cell lies in the first-layer tails: the single-cell dragging disrupts the lattice with more than two tail cells, while the double-drag configuration has exactly two, which facilitates later healing of defects (Appendix Fig. 24(b)). We can also compare different force angles  $\Psi_d$  in the single-cell drag simulations. For  $\Psi_d = 0^\circ$ , we observe a distinctive first layer of defect cells contacting the core cells, and it comprises -L defects, which are accompanied by a second layer of +L defects (Fig. 7(b)). As  $\Psi_d$  increases, the lattice defect structure undergoes a significant transformation (Fig. 7(c,d)). Specifically, in the wake region, the well-structured pattern with clear +L-defect regions at  $\Psi_d = 0^\circ$  evolves into a ‘flame’ pattern characterized by a blur center of +L defects surrounded by -L-defect cells. This structural transition is pronounced when  $\Psi_d \rightarrow 30^\circ$  (Fig. 7d). For intermediate drag angles ( $0^\circ < \Psi_d < 30^\circ$ ), the defect pattern in the tail region breaks axial symmetry, with more

+L defects on the left side of the dragged cell and more −L defects on the right side (Fig. 7c).

The difference in wake defects between single-cell and double-cell drag simulations can also be understood by examining the spatial distributions of defect cells and T1 transition events (Appendix Fig. 24(a), SM movie 5). In both scenarios, abundant T1 transition events can be found in front of and behind the dragged cell(s), which is attributed to its or their constant displacement with respect to the surrounding cells (Appendix Fig. 24(a)). In the single-cell drag simulation, T1 transitions occur intensively right behind the dragged cell, but emerge uniformly in the wake region, giving rise to scattered L defects (Appendix Fig. 24(a)); whereas in the double-cell drag simulation, T1 transitions happen frequently right behind the follower cell and also at the positions of the winglet cells (Appendix Fig. 24(a, b)). The inhomogeneous spatial distribution of T1 transitions in the double-cell drag scenario is consistent with the fact that the two winglet cells and the follower cell are involved in the auto-healing process of wake defects.

Our cell drag simulations have biological relevance. Collective cell migration, a cornerstone of biological processes such as tissue repair, embryonic morphogenesis, and cancer metastasis [78–80], frequently adopts a *leader-follower* topological configuration to sustain persistent directional movement [81]. While prior studies have predominantly focused on biochemical signaling as the regulatory framework for such collective behavior—particularly in contexts like wound healing and tumor invasion [82]—our findings highlight the mechanical origin. We demonstrate that microscale auto-healing *leader-follower* architecture, without any biochemical guidance cues, is sufficient to drive ordered collective migration through purely mechanical interactions. This mechanical perspective complements existing biochemical models, suggesting that the physical arrangement of cells and their force transmission dynamics can alternatively facilitate cell migration even in the absence of biochemical signaling pathways.

In summary, our work provides new physical insight for understanding the complex dynamics of active confluent tissues and clarifying the roles of lattice and orientational defects in steady state and during cellular transport. Importantly, we have predicted a possible way of defect-free cell migration without any biochemical coordination between cells. During this cell migration process, defect cells annihilate in a nontrivial spatiotemporal pattern. This prediction can be heuristic for the further understanding of cellular transport during many physiological processes, such as wound healing and cancer metastasis, in which stem cells and cancer cells can migrate while preserving tissue integrity. Future works can be devoted to three-dimensional simulations as well as how biochemical factors and extra cellular matrix can contribute to the collective transport of cells.

## VI. ACKNOWLEDGEMENT

This work is supported by the Research Grants Council of Hong Kong via grant number 16300221 and NSFC–RGC

Joint Research Scheme N\_HKUST627/23. We gratefully acknowledge inspiring discussions with Prof. Tiezheng Qian on solid-liquid transitions and valuable inputs from Prof. Greg Huber regarding drag simulation. We are indebted to Prof. Rastko Sknepnek for his expert guidance on lattice statistics and suggestions for model refinement, and to Prof. Dapeng Bi for fruitful discussions on lattice defect annihilation. Special thanks go to Dr. Lakshmi Balasubramaniam for providing critical experimental evidence and engaging discussions and Prof. Luca Giomi for helpful and encouraging suggestions. We also extend our appreciation to Prof. Yun Chang for sharing helpful biological perspective on our results, and to Profs. Liting Duan and Qun-Li Lei for their constructive suggestions and perspectives. Furthermore, we thank Zeyang Mou, Wentao Tang, Haijie Ren, and Zeming Liu for their stimulating discussions and contributions.

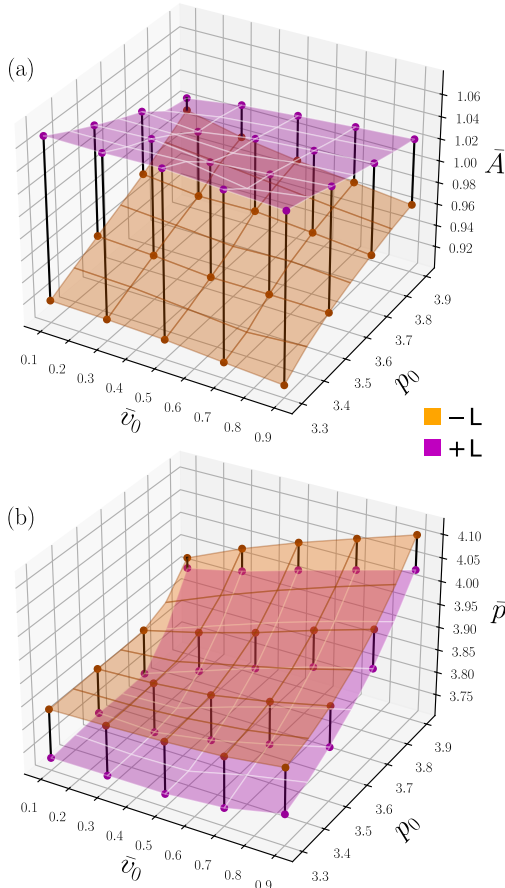


FIG. 8. 3D plot of (a) the ensemble-average of cell area,  $\bar{A}$ , and (b) the ensemble-average of cell shape parameter,  $\bar{p}$ , for +L defects (purple) and -L defects (yellow) with  $0.1 \leq \bar{v}_0 \leq 0.9$  and  $3.3 \leq p_0 \leq 3.95$ .

#### Appendix A: Director field interpolation

For defect motion analysis, we use a resolution of  $150 \times 150$  for the simulation box with the pixel size of  $0.2 \times 0.2$ . We apply a Gaussian filter ( $\sigma = 5$ ;  $dx = \sigma\delta = 1$ ) to the  $\mathbf{Q}$ -tensor field, smoothing scales slightly larger than the cell diameter [43]. This suppresses overfitting artifacts while preserving defect topology, enabling reliable director field reconstruction and defect detection for quantitative analysis (Fig. 1) [69].

#### Appendix B: Orientational defect orientation detection

For a single defect, the orientation of the surrounding directors can be written as:

$$\theta = k\phi + \theta_0, \quad (\text{B1})$$

where  $k$  is the winding number of the defect,  $\phi$  is the azimuthal angle of the surrounding director relative to the  $x$ -axis, and  $\theta_0$  is the characteristic angle of the defect [83]. The following equations are used to calculate the orientation of

defects with  $k \neq +1$ :

$$\Phi_k = \frac{\theta_0}{2(1-k)} \pmod{\frac{\pi}{|1-k|}}, \quad (\text{B2})$$

$$\Phi_{+1/2} = 2\theta_0 \pmod{2\pi}, \quad (\text{B3})$$

$$\Phi_{-1/2} = 2\theta_0/3 \pmod{2\pi/3}, \quad (\text{B4})$$

where angle  $\Phi_k$  characterizes the orientation of the defect with topological charge  $k$ . For a  $k = +1/2$  defect,  $\Phi_{+1/2}$  points towards the tail, while for a  $k = -1/2$  defect,  $\Phi_{-1/2}$  points towards one of its branches that are  $\frac{2\pi}{3}$  apart. Then the head direction of  $+1/2$  defects is  $\phi_{+1/2} = \Phi_{+1/2} \pm \pi$ .

#### Appendix C: The hexatic order

The analysis of  $z$  (Appendix Fig. 10) and the statistics of the hexatic order in (Appendix Fig. 9, Appendix Fig. 11) reveal that the system reaches its lowest density of L defects and exhibits the strongest hexatic order in the cell arrangement in the vicinity of the solid-liquid transition. This phenomenon, commonly referred to as the hexatic phase, has been previously observed in both theoretical and numerical studies [53, 55, 56, 72].

At low motility, below the transition point, cells lack the energy to overcome the confinement of their neighbors. Consequently, the system remains in a disordered solid state characterized by a persistently high density of L defects and low hexatic order.

As motility increases to the critical point, cells gain sufficient energy to overcome the barrier for neighbor exchanges (T1 transitions). This enables the system to annihilate L defects present in the initial disordered state and promotes the formation of the hexatic order. This defect annihilation and alignment lead to a distinct peak in the hexatic order and a corresponding minimum in the L defect density, marking the emergence of the hexatic phase.

Further increasing motility beyond the critical point removes the energetic restriction on T1 transitions. This fluidity disrupts spatial order, facilitating the generation of new L defects (disclinations and dislocations). Consequently, L defect density rises while hexatic order declines.

The hexatic phase is thus identified as the intermediate state between the solid and liquid phases. We determine the  $p_0$  transition points for different  $\bar{v}_0$  by locating the characteristic peaks in both hexagonal packing count and hexatic order parameter (Fig. 11), consistent with established findings [25].

#### Appendix D: L defect lifetime

We find that the lifetime distributions of the L defects follow an exponential function in both liquid and solid states, where we see a linear relation in  $n_L \propto e^{-\lambda t}$  (Appendix Fig. 12). So we can calculate the half life of the L defects by  $t_{1/2} = \frac{\ln 2}{\lambda}$  (Appendix Fig. 13). When the system can flow and cells are soft enough to undergo deformation and neighbor exchange, lattice defects exhibit shorter life time. The lifetime

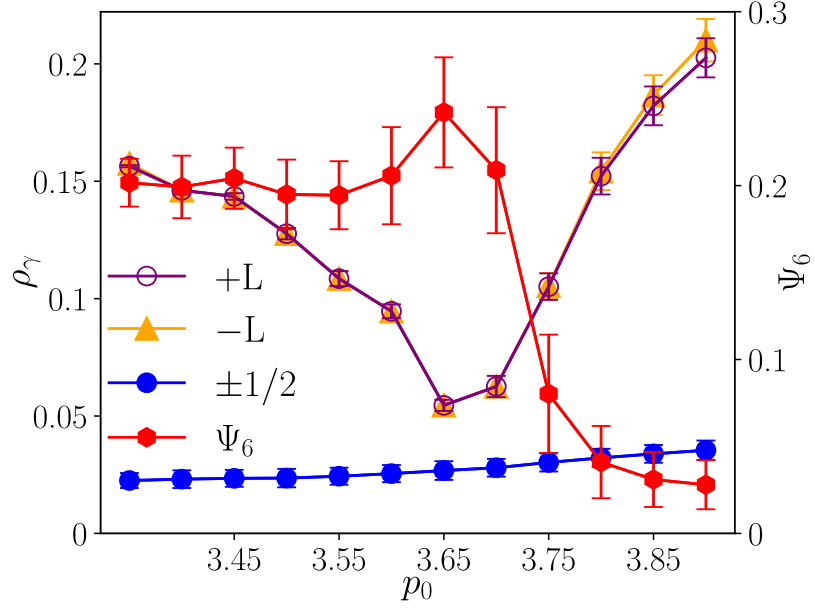


FIG. 9. The density of lattice and orientational defects  $\rho_\gamma$  as a function of  $p_0$ , where  $\gamma = +L, -L, +1/2$ , or  $-1/2$ .  $\Psi_6$  is the hexatic order.  $\bar{v}_0 = 0.3$  is fixed.

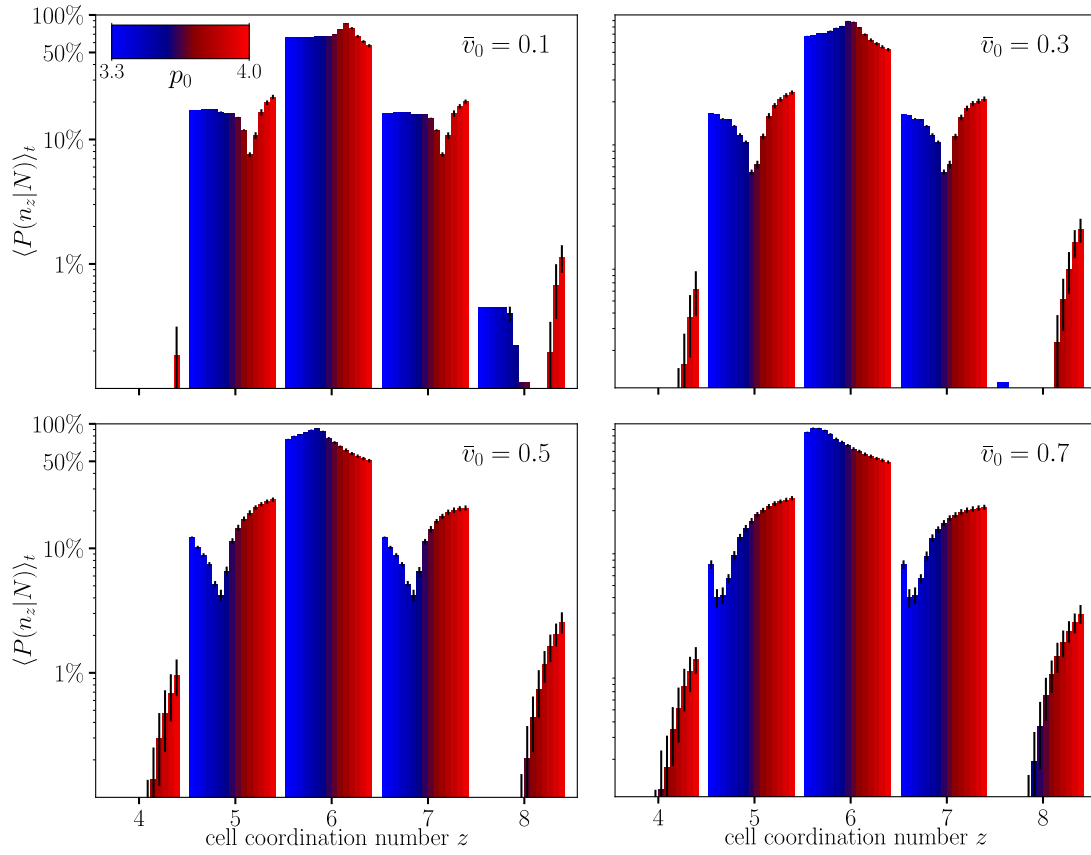


FIG. 10. Number distribution of cells  $\langle P(n_z|N) \rangle_t$  as a function of coordination number  $z$  with various  $\bar{v}_0$  and  $p_0$ . The peaks of  $z = 6$  move together with the valley of  $z = 5$  and  $z = 7$  to the lower  $p_0$  with higher  $\bar{v}_0$ .

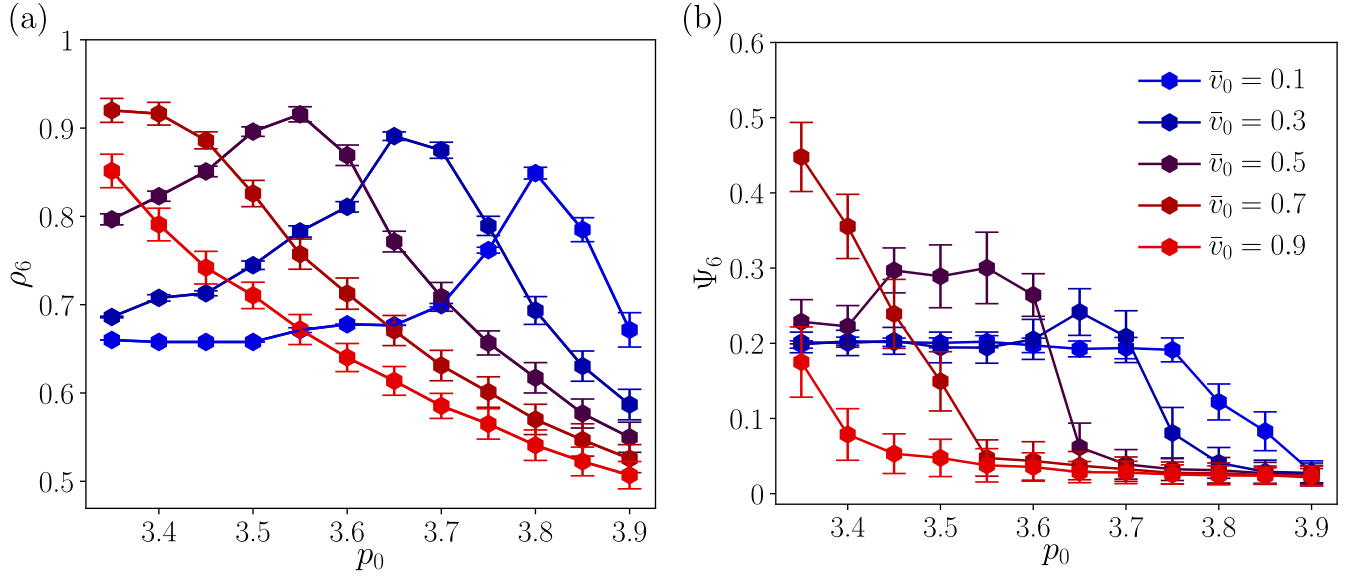


FIG. 11. (a) The density of hexagons  $\rho_6$  and (b) the hexatic order of the tissues with various  $\bar{v}_0$  and  $p_0$ . The peaks indicate the hexatic phase.

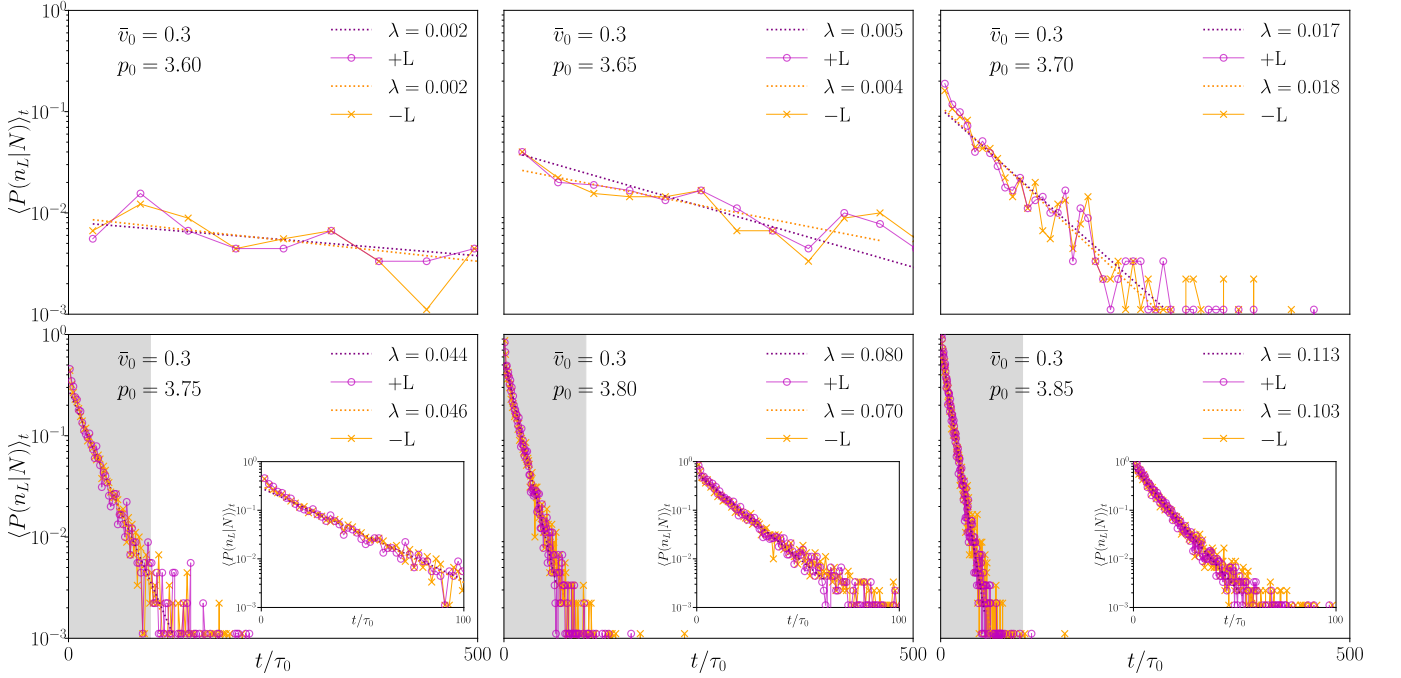


FIG. 12. Lifetime distribution of L defects at  $\bar{v}_0 = 0.3$  and variable  $p_0 \in [3.6, 3.85]$ , in which we observe  $n_L \propto e^{-\lambda t}$ . The half-life of the lattice defects is  $t_{1/2} = \frac{\ln 2}{\lambda}$ . Gray regions corresponds to the insets.

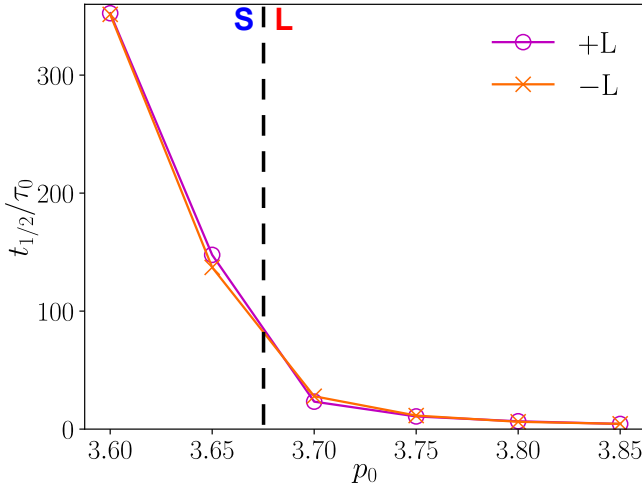


FIG. 13. The half life of L defects at  $\bar{v}_0 = 0.3$  against  $p_0$ .

statistics give us a proper way to characterize how active the cell rearrange and migrate in the system and also a good way to distinguish liquid and solid states (Appendix Fig. 13).

#### Appendix E: Detailed nematic analysis

In the analysis of the motion of  $+1/2$  defects, we track their positions over time, considering various defect lifetimes. Defects were categorized by lifetime thresholds ( $\tau_L/\tau_0$ ; Appendix Fig. 14(a–c)), distinguishing two behavioral regimes. Short-lived defects predominantly form transient bonded pairs with  $-1/2$  defects that undergo fluctuation-driven formation/annihilation, exhibiting symmetric motion pathways without consistent head/tail orientation. Conversely, long-lived defects remain unbonded and mobile, displaying phase-dependent extensile behavior: pronounced in liquid phase but significantly suppressed in solid phase.

Statistical analysis of long-lived defect trajectories during aging intervals ( $s < t/\tau_0 < s + 1$ ;  $s = 0, 1, 2$ ; Appendix Fig. 14d–f) demonstrated that  $+1/2$  defects progressively unbind and develop stronger extensile character as they age in the liquid phase.

These results establish lifetime-dependent nematic behavior: nascent and short-lived defects exhibit thermal-fluctuation-dominated motion within bonded pairs, while aged/long-lived defects show marked phase contrast in extensile character. The liquid-phase enhancement arises from global cell migration, rapid rearrangement, and local structural variation, showing the important role of nematic behavior in tissue dynamics.

#### Appendix F: Experimental evidence of spatio-orientational correlation

Our simulation findings of the spatio-orientational correlation between lattice and orientational defects are further sup-

ported by experimental evidence. Appendix Fig. 15 shows the spatial distribution of L and  $+1/2$  defects identified in epithelial tissues from three independent studies [18, 40, 75]. Consistent with our simulations,  $+L$  defects are predominantly located near the head of  $+1/2$  defects, while  $-L$  defects are found at their tail. These observations validate our results and demonstrate a strong correlation between nematic behavior at the mesoscopic level and cell rearrangements, or hexatic order, at the cellular level.

#### Appendix G: Drag configurations

To realize the auto-healing process we tried several drag configurations: drag one cell continuously in a periodic box; drag one cell back and forth; drag two cells in the same height horizontally with opposite directions; drag two nearby cells horizontally; drag two distant cells (Appendix Fig. 19). We examine the lattice defects to identify the auto healing where we find the only configuration that auto heals the L defects is the dragging of two nearby cells. The wake region can restore the hexatic order with two first-layer rows of cells displaced by one lattice constant  $a$  (Appendix Fig. 19(d)). We observed minimized displacement compared with other configurations and only leave L defects at the starting and ending positions. The auto-healing process is noise tolerant stable and reproducible. In together 3 cells in a packet is far transferred with two following rows advanced one position.

#### Appendix H: Auto-healing mechanism

Defect evolution in the double-cell drag simulation is governed by two mechanisms. The  $+L$  defects in the outer regions (Cells A, B, C, D, E) propagate synchronously with the packet (Appendix Fig. 20(b–d)). The multicellular structure exhibits laterally positioned  $+L$ -defect winglet cells that move in synchrony during locomotion. Simultaneously,  $+L$  defects at the tail of the first layer cells (Cells X, Y, Z) “wagging”, neutralizing the  $-L$  defects and ultimately healing all L defects and restoring hexagonal order (Appendix Fig. 20(b–f)). This neutralization mirrors the reverse mechanism of  $-L$  tail generation at the head of the packet, completing the cycle of defect generation and annihilation.

#### Appendix I: Free energy spectrum

To analyze the nontrivial periodicity of the auto-healing process of double-cell dragging simulation, we examine the energy variation. We track the total free energy  $E_{\text{total}} = E_{\text{AVM}}$  over time, focusing on two terms: the cell area term,  $E_A = \sum_{i=1}^N \frac{K}{2} (A_i - A_0)^2$ , and the cell perimeter term,  $E_P = \sum_{i=1}^N \frac{\Gamma}{2} (P_i - P_0)^2$  (Appendix Fig. 21). For configurations other than the double-cell drag scenario, the total free energy increases over time due to the continuous introduction of L defects into the system. In anti-aligned and distant-aligned

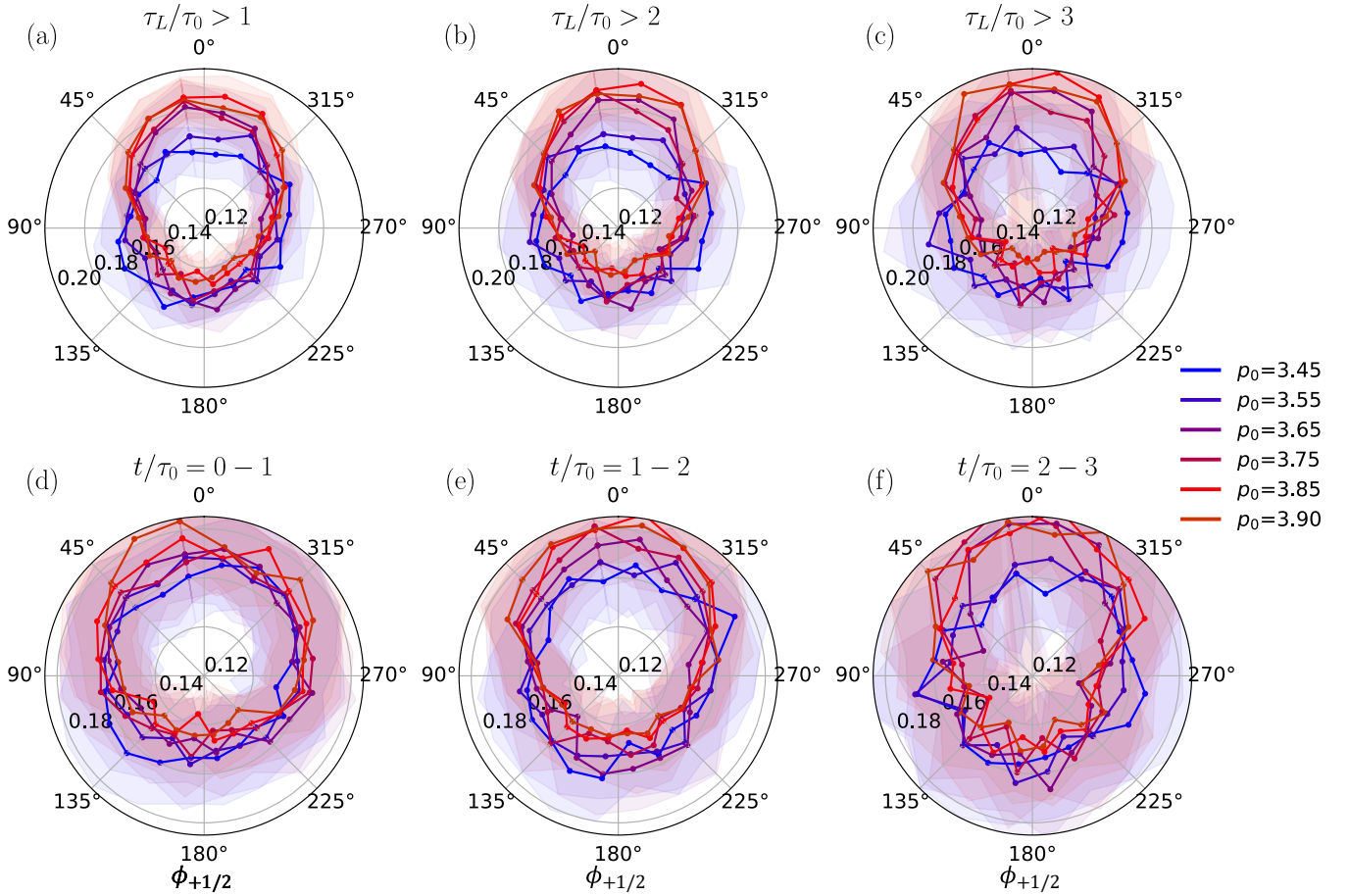


FIG. 14. (a–c) Rose-plot of  $\phi_{+1/2}$  with different lifetime  $\tau_L$  of the  $+1/2$  defects. (d–f) Rose-plot of  $\phi_{+1/2}$  in different ages of the  $+1/2$  defects.

configurations,  $E_{\text{total}}$  approximately doubles the free energy of single cell configurations, as the two driven cells generate twice as many L defects without achieving auto-healing. Due to the incompressibility of the system,  $E_A$  converges for all configurations once the system is in a steady-like state. In contrast,  $E_P$  is more closely linked to the L defects, contributing to the differences between the auto-healing configuration and others. While fluctuations in  $E_P$  occur for all configurations, the auto-healing configuration exhibits periodic-like oscillations.

We perform a Fourier transform over all energy terms and

identify a ubiquitous significant period  $T_{f_1}/\tau_0 = 0.57$ , which is particularly present in the  $E_P$  spectrum (Appendix Fig. 22). Given the average speed  $\bar{v} = 4.68$  of the moving packet in the simulation, the characteristic period is  $T_0/\tau_0 = \frac{a}{\bar{v}} \approx 0.23$ . While the trivial period  $T_{f_2} \approx T_0$  also emerges, the dominant  $T_{f_1} \approx 2.5T_0$  reflects the nontrivial periodicity arising from the auto-healing process. Specifically, the coordination number  $z$  of the follower cell, dynamically modified by its T1 transitions, also exhibits a dominant period  $T_{f_1}$ . This suggests that the spatial distribution of the T1 transition events and the temporal behavior of the follower cell's coordination number underlie the nontrivial period  $2.5T_0$  of the moving packet.

- 
- [1] T. E. Angelini, E. Hannezo, X. Trepate, J. J. Fredberg, and D. A. Weitz, Cell migration driven by cooperative substrate deformation patterns, *Physical Review Letters* **104**, 168104 (2010).
  - [2] A. Puliafito, L. Hufnagel, P. Neveu, S. Streichan, A. Sigal, D. K. Fygenson, and B. I. Shraiman, Collective and single cell behavior in epithelial contact inhibition, *Proceedings of the National Academy of Sciences* **109**, 739 (2012).
  - [3] F. Jülicher, S. W. Grill, and G. Salbreux, Hydrodynamic the-

ory of active matter, *Reports on Progress in Physics* **81**, 076601 (2018).

- [4] R. Alert and X. Trepate, Physical models of collective cell migration, *Annual Review of Condensed Matter Physics* **11**, 77 (2020).
- [5] S. Banerjee and M. C. Marchetti, Continuum models of collective cell migration, in *Cell Migrations: Causes and Functions*, edited by C. A. M. La Porta and S. Zapperi (Springer Interna-

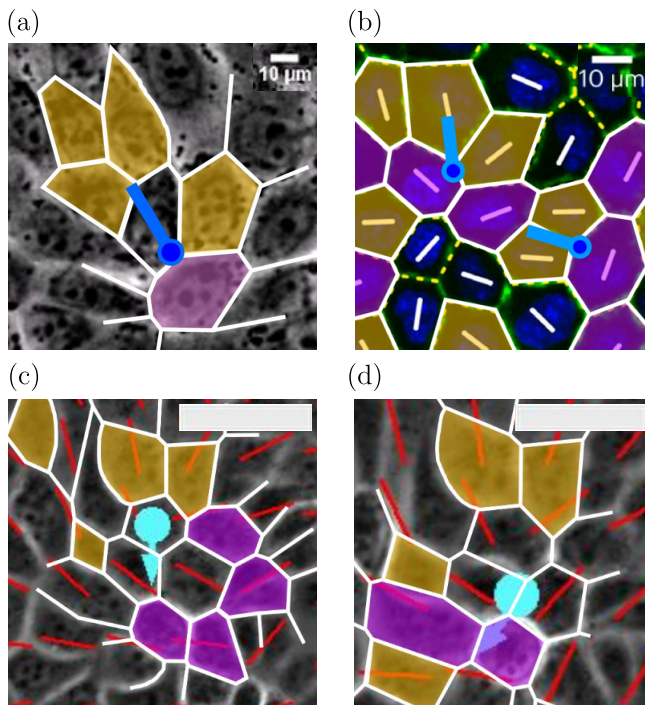


FIG. 15. The experimental evidence of spatio-orientational correlation between L and  $+1/2$  defects. (a, b) The blue bars indicate the tail direction of  $+1/2$  defects, (c, d) the cyan arrows denote the head direction of  $+1/2$  defects taken from the original video frame. (a) is from SI video snapshot of Saw et al. work [18]; (b) is from the Fig. 1 of Armengol-Collado et al. work [75]; (c, d) are from the supplementary video 1 frame of the work from Balasubramaniam et al. [40], scale bar:  $50 \mu\text{m}$ .

- tional Publishing, Cham, 2019) pp. 45–66.
- [6] X. Trepata, M. R. Wasserman, T. E. Angelini, E. Millet, D. A. Weitz, J. P. Butler, and J. J. Fredberg, Physical forces during collective cell migration, *Nature Physics* **5**, 426 (2009).
  - [7] M. Deforet, V. Hakim, H. G. Yevick, G. Duclos, and P. Silberzan, Emergence of collective modes and tri-dimensional structures from epithelial confinement, *Nature Communications* **5**, 3747 (2014).
  - [8] R. Mueller, J. M. Yeomans, and A. Doostmohammadi, Emergence of active nematic behavior in monolayers of isotropic cells, *Physical Review Letters* **122**, 048004 (2019).
  - [9] C. Blanch-Mercader, V. Yashunsky, S. Garcia, G. Duclos, L. Giomi, and P. Silberzan, Turbulent dynamics of epithelial cell cultures, *Physical Review Letters* **120**, 208101 (2018).
  - [10] J.-Q. Lv, P.-C. Chen, Y.-P. Chen, H.-Y. Liu, S.-D. Wang, J. Bai, C.-L. Lv, Y. Li, Y. Shao, X.-Q. Feng, and B. Li, Active hole formation in epithelioid tissues, *Nature Physics* **20**, 1313 (2024).
  - [11] D. J. Cisló, F. Yang, H. Qin, A. Pavlopoulos, M. J. Bowick, and S. J. Streichan, Active cell divisions generate fourfold orientationally ordered phase in living tissue, *Nature Physics* **19**, 1201 (2023).
  - [12] J. Rozman and J. M. Yeomans, Cell sorting in an active nematic vertex model, *Physical Review Letters* **133**, 248401 (2024).
  - [13] P. Friedl and D. Gilmour, Collective cell migration in morphogenesis, regeneration and cancer, *Nature Reviews Molecular Cell Biology* **10**, 445 (2009).
  - [14] A. Brugués, E. Anon, V. Conte, J. H. Veldhuis, M. Gupta, J. Colombelli, J. J. Muñoz, G. W. Brodland, B. Ladoux, and X. Trepata, Forces driving epithelial wound healing, *Nature Physics* **10**, 683 (2014).
  - [15] A. Pasupalak, Z. Wu, and M. P. Ciamarra, Epithelial tissues from the bottom-up: Contact inhibition, wound healing, and force networks, *arXiv [cond-mat.soft]* (2024).
  - [16] E. H. Barriga, K. Franze, G. Charras, and R. Mayor, Tissue stiffening coordinates morphogenesis by triggering collective cell migration in vivo, *Nature* **554**, 523 (2018).
  - [17] Y.-W. Li, Y. Yao, and M. P. Ciamarra, Two-dimensional melting of two- and three-component mixtures, *Physical Review Letters* **130**, 258202 (2023).
  - [18] T. B. Saw, A. Doostmohammadi, V. Nier, L. Kocgozlu, S. Thampi, Y. Toyama, P. Marcq, C. T. Lim, J. M. Yeomans, and B. Ladoux, Topological defects in epithelia govern cell death and extrusion, *Nature* **544**, 212 (2017).
  - [19] C. F. Guimarães, L. Gasperini, A. P. Marques, and R. L. Reis, The stiffness of living tissues and its implications for tissue engineering, *Nature Reviews Materials* **5**, 351 (2020).
  - [20] T. E. Angelini, E. Hannezo, X. Trepata, M. Marquez, J. J. Fredberg, and D. A. Weitz, Glass-like dynamics of collective cell migration, *Proceedings of the National Academy of Sciences* **108**, 4714 (2011).
  - [21] A. Haeger, M. Krause, K. Wolf, and P. Friedl, Cell jamming: Collective invasion of mesenchymal tumor cells imposed by tissue confinement, *Biochimica et Biophysica Acta (BBA) - General Subjects* **1840**, 2386 (2014).
  - [22] J. P. Chen, R. Li, J. X. Jiang, and X.-D. Chen, Autocrine factors produced by mesenchymal stem cells in response to cell–cell contact inhibition have anti-tumor properties, *Cells* **12**, 2150 (2023).
  - [23] J. P. Thiery, Epithelial–mesenchymal transitions in tumour progression, *Nature Reviews Cancer* **2**, 442 (2002).
  - [24] E. W. Thompson and D. F. Newgreen, Carcinoma invasion and metastasis: A role for epithelial-mesenchymal transition?, *Cancer Research* **65**, 5991 (2005).
  - [25] D. Bi, X. Yang, M. C. Marchetti, and M. L. Manning, Motility-driven glass and jamming transitions in biological tissues, *Physical Review X* **6**, 021011 (2016).
  - [26] M. Chiang and D. Marenduzzo, Glass transitions in the cellular potts model, *Europhysics Letters* **116**, 28009 (2016).
  - [27] D. L. Barton, S. Henkes, C. J. Weijer, and R. Sknepnek, Active vertex model for cell-resolution description of epithelial tissue mechanics, *PLOS Computational Biology* **13**, e1005569 (2017).
  - [28] S. Tong, N. K. Singh, R. Sknepnek, and A. Košmrlj, Linear viscoelastic properties of the vertex model for epithelial tissues, *PLOS Computational Biology* **18**, e1010135 (2022).
  - [29] M. J. Hertaeg, S. M. Fielding, and D. Bi, Discontinuous shear thickening in biological tissue rheology, *Physical Review X* **14**, 011027 (2024).
  - [30] A. Hopkins, M. Chiang, B. Loewe, D. Marenduzzo, and M. C. Marchetti, Local yield and compliance in active cell monolayers, *Physical Review Letters* **129**, 148101 (2022).
  - [31] S.-Z. Lin, Y. Li, J. Ji, B. Li, and X.-Q. Feng, Collective dynamics of coherent motile cells on curved surfaces, *Soft Matter* **16**, 2941 (2020).
  - [32] L.-b. Cai, W. Ji, J. Luo, Q.-l. Lei, and Y.-q. Ma, Numerical study of dynamic zigzag patterns in migrating epithelial tissue, *Science China Physics, Mechanics & Astronomy* **65**, 217011 (2021).
  - [33] D. Bi, J. H. Lopez, J. M. Schwarz, and M. L. Manning, A density-independent rigidity transition in biological tissues, *Nature Physics* **11**, 1074 (2015).

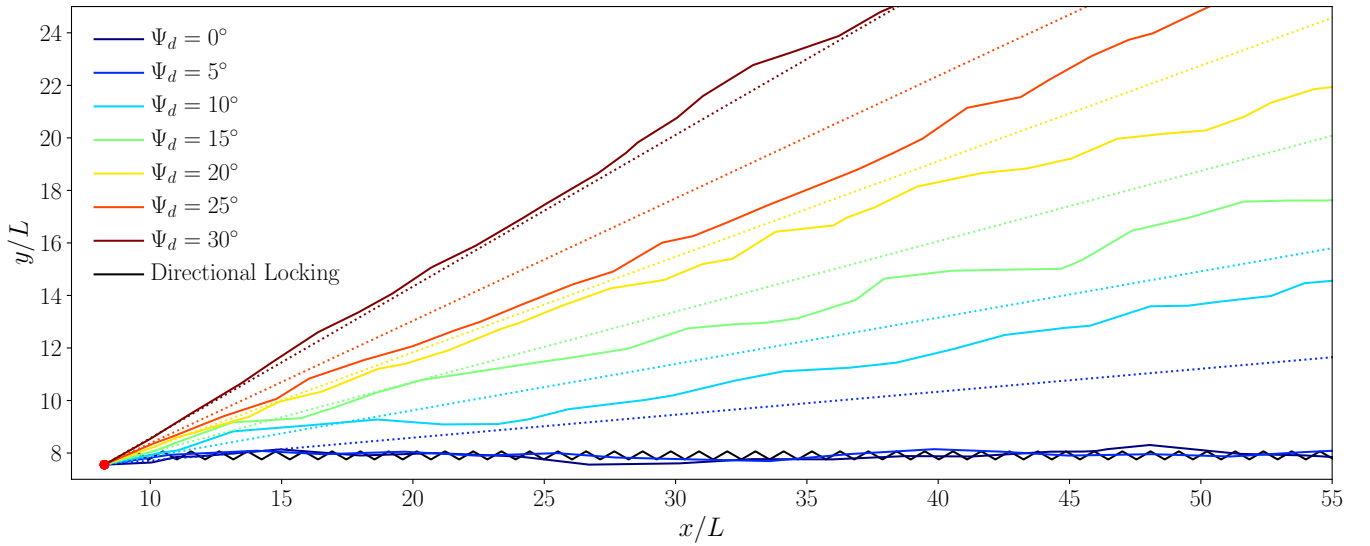


FIG. 16. The trajectories of the dragged cell at different  $\Psi_d$ . The force direction is indicated by the dotted line. The black line gives the directional locking path in the hexagonal lattice.

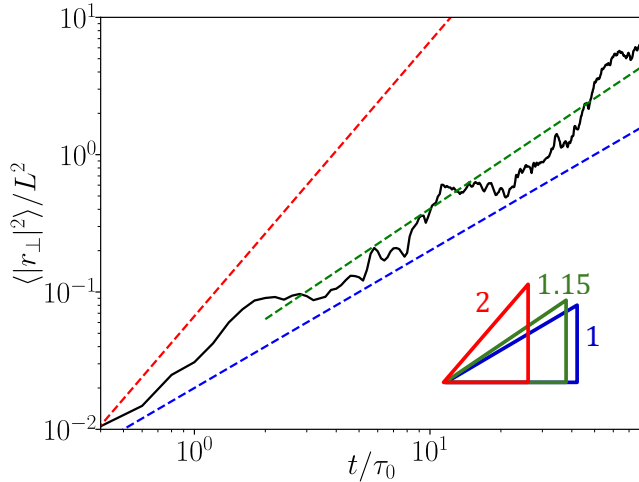


FIG. 17. The mean squared displacement of the dragged cell at  $\Psi_d = 30^\circ$  along the direction perpendicular to the force angle at  $\bar{F}_d = 6$ . The triangles indicate the exponents of the corresponding color line.

[34] S. Kim, R. Amini, S.-T. Yen, P. Pospíšil, A. Boutillon, I. A. Deniz, and O. Campàs, A nuclear jamming transition in vertebrate organogenesis, *Nature Materials* **23**, 1592 (2024).  
 [35] G. Duclos, C. Erlenkämper, J.-F. Joanny, and P. Silberzan, Topological defects in confined populations of spindle-shaped cells, *Nature Physics* **13**, 58 (2017).  
 [36] K. Kawaguchi, R. Kageyama, and M. Sano, Topological defects control collective dynamics in neural progenitor cell cultures, *Nature* **545**, 327 (2017).  
 [37] A. Doostmohammadi, J. Ignés-Mullol, J. M. Yeomans, and F. Sagués, Active nematics, *Nature Communications* **9**, 3246 (2018).  
 [38] R. Zhang, A. Mozaffari, and J. J. de Pablo, Autonomous materials systems from active liquid crystals, *Nature Reviews Materials* **6**, 437 (2021).

[39] T. B. Saw, W. Xi, B. Ladoux, and C. T. Lim, Biological tissues as active nematic liquid crystals, *Advanced Materials* **30**, 1802579 (2018).  
 [40] L. Balasubramaniam, A. Doostmohammadi, T. B. Saw, G. H. N. S. Narayana, R. Mueller, T. Dang, M. Thomas, S. Gupta, S. Sonam, A. S. Yap, Y. Toyama, R.-M. Mège, J. M. Yeomans, and B. Ladoux, Investigating the nature of active forces in tissues reveals how contractile cells can form extensile monolayers, *Nature Materials* **20**, 1156 (2021).  
 [41] D. Dell'Arciprete, M. L. Blow, A. T. Brown, F. D. C. Farrell, J. S. Lintuvuori, A. F. McVey, D. Marenduzzo, and W. C. K. Poon, A growing bacterial colony in two dimensions as an active nematic, *Nature Communications* **9**, 4190 (2018).  
 [42] F. Vafa, M. J. Bowick, B. I. Shraiman, and M. C. Marchetti, Fluctuations can induce local nematic order and extensile stress in monolayers of motile cells, *Soft Matter* **17**, 3068 (2021).  
 [43] A. Killeen, T. Bertrand, and C. F. Lee, Polar fluctuations lead to extensile nematic behavior in confluent tissues, *Physical Review Letters* **128**, 078001 (2022).  
 [44] L. A. Hoffmann, L. N. Carenza, J. Eckert, and L. Giomi, Theory of defect-mediated morphogenesis, *Science Advances* **8**, eabk2712 (2022).  
 [45] Y. Maroudas-Sacks, L. Garion, L. Shani-Zerbib, A. Livshits, E. Braun, and K. Keren, Topological defects in the nematic order of actin fibres as organization centres of hydra morphogenesis, *Nature Physics* **17**, 251 (2021).  
 [46] S. Monfared, G. Ravichandran, J. Andrade, and A. Doostmohammadi, Mechanical basis and topological routes to cell elimination, *eLife* **12**, e82435 (2023).  
 [47] G. Zhang and J. M. Yeomans, Active forces in confluent cell monolayers, *Physical Review Letters* **130**, 038202 (2023).  
 [48] S. Yamada, S. Pokutta, F. Drees, W. I. Weis, and W. J. Nelson, Deconstructing the cadherin-catenin-actin complex, *Cell* **123**, 889 (2005).  
 [49] S. A. Sandersius, M. Chuai, C. J. Weijer, and T. J. Newman, Correlating cell behavior with tissue topology in embryonic epithelia, *PLOS ONE* **6**, e18081 (2011).

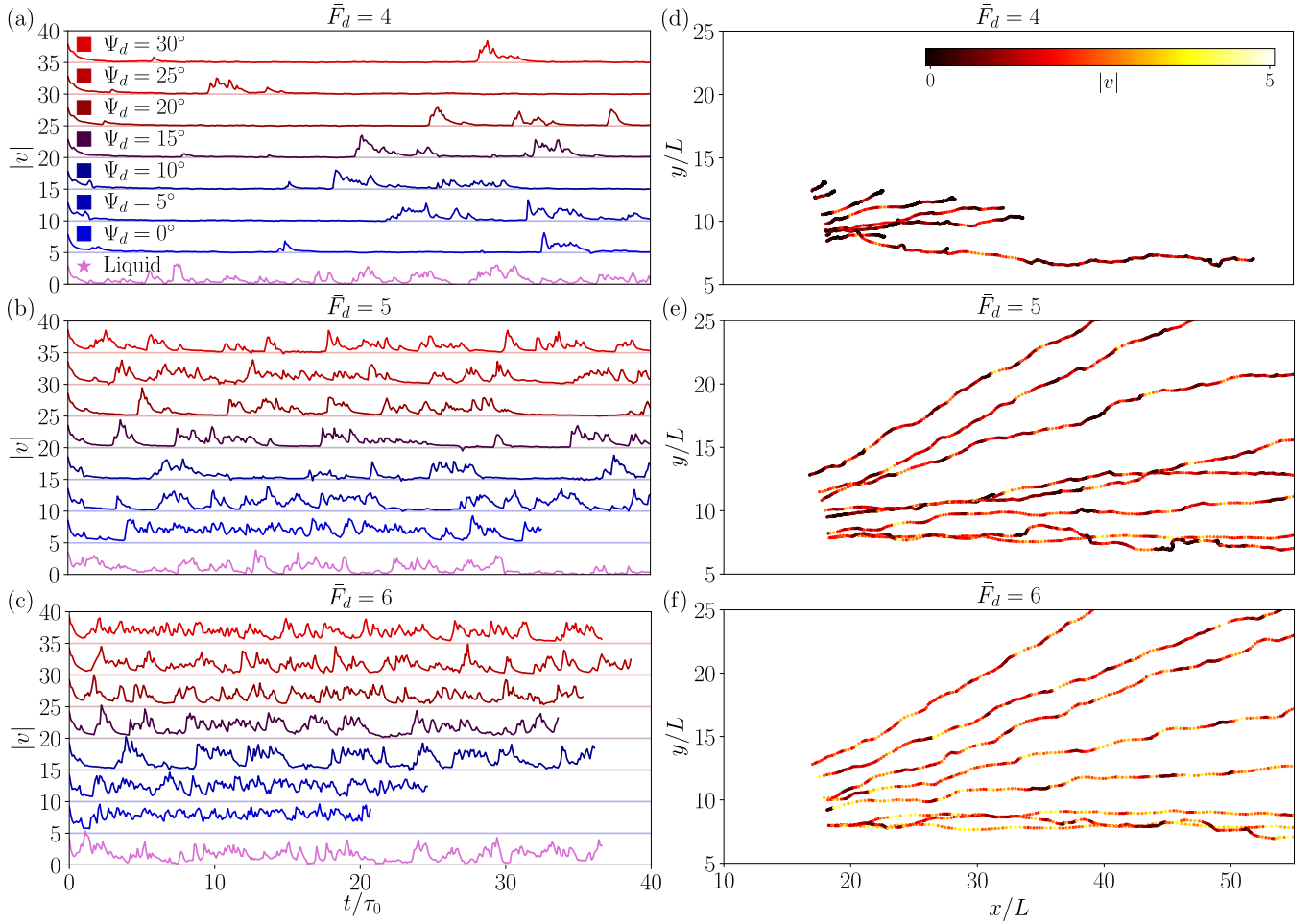


FIG. 18. Stick-slip behavior of the dragged cell. (a–c) The speed  $|v|$  of the dragged cell along the mean path as a function of time, with various  $\Psi_d$  in the liquid state. The curves are vertically offset by 5 for clarity. A reference line of the same color is included for comparison. The zig-zag pattern indicates stick-slip motion in these cases. The trajectory starts when dragging is initiated and ends when the cell travels a distance of  $L_{\max} = 60$ . (d–f) Trajectories of the dragged cell in a hexagonal lattice at different angles, each starting  $10L$  from the origin. Colors represent the speed along the mean path.

- [50] D. S. Roshal, K. Azzag, E. Le Goff, S. B. Rochal, and S. Baghdiguian, Crystal-like order and defects in metazoan epithelia with spherical geometry, *Scientific Reports* **10**, 7652 (2020).
- [51] A. Z. Jennifer and Z. Richard, Cell-pattern disordering during convergent extension in drosophila, *Journal of Physics: Condensed Matter* **16**, S5073 (2004).
- [52] A.-K. Classen, K. I. Anderson, E. Marois, and S. Eaton, Hexagonal packing of drosophila wing epithelial cells by the planar cell polarity pathway, *Developmental Cell* **9**, 805 (2005).
- [53] Y. Tang, S. Chen, M. J. Bowick, and D. Bi, Cell division and motility enable hexatic order in biological tissues, *Physical Review Letters* **132**, 218402 (2024).
- [54] A. Pasupalak, L. Yan-Wei, R. Ni, and M. Pica Ciamarra, Hexatic phase in a model of active biological tissues, *Soft Matter* **16**, 3914 (2020).
- [55] M. Durand and J. Heu, Thermally driven order-disorder transition in two-dimensional soft cellular systems, *Physical Review Letters* **123**, 188001 (2019).
- [56] Y.-W. Li and M. P. Ciamarra, Role of cell deformability in the two-dimensional melting of biological tissues, *Physical Review Materials* **2**, 045602 (2018).
- [57] J. Rozman, J. M. Yeomans, and R. Sknepnek, Shape-tension coupling produces nematic order in an epithelium vertex model, *Physical Review Letters* **131**, 228301 (2023).
- [58] Y.-W. Li, L. L. Y. Wei, M. Paoluzzi, and M. P. Ciamarra, Softness, anomalous dynamics, and fractal-like energy landscape in model cell tissues, *Physical Review E* **103**, 022607 (2021).
- [59] B. Loewe, M. Chiang, D. Marenduzzo, and M. C. Marchetti, Solid-liquid transition of deformable and overlapping active particles, *Physical Review Letters* **125**, 038003 (2020).
- [60] M. Chiang, A. Hopkins, B. Loewe, M. C. Marchetti, and D. Marenduzzo, Intercellular friction and motility drive orientational order in cell monolayers, *Proceedings of the National Academy of Sciences* **121**, e2319310121 (2024).
- [61] N. Noll, M. Mani, I. Heemskerk, S. J. Streichan, and B. I. Shraiman, Active tension network model suggests an exotic mechanical state realized in epithelial tissues, *Nature Physics* **13**, 1221 (2017).
- [62] M. Durand and J. Heu, Thermally driven order-disorder transition in two-dimensional soft cellular systems, *Physical Review Letters* **123**, 188001 (2019).

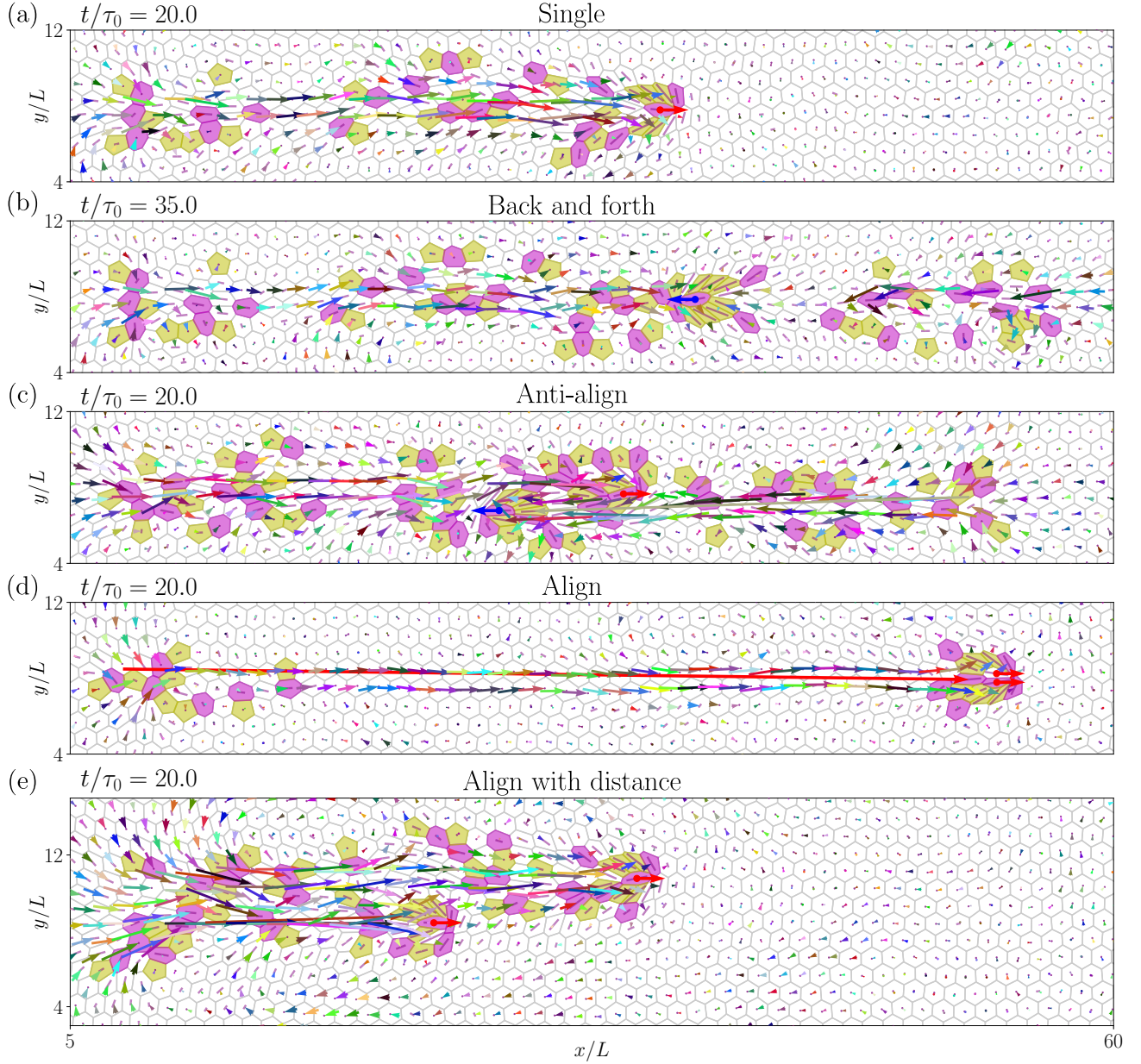


FIG. 19. The wake defect structure for different cell drag simulations: (a) drag one cell horizontally; (b) drag one cell back and forth; (c) drag two cells in different regions in the opposite direction; (d) drag two nearby cells in the same direction; (e) drag two distant cells in the same direction. The arrows indicate the displacement field. The motility of all driven cells is horizontal at  $\Psi_d = 0^\circ$  indicated by the red arrow, and indicated by the blue arrow for the reverse direction.

- [63] J. Rozman, K. V. S. Chaithanya, J. M. Yeomans, and R. Sknepnek, Vertex model with internal dissipation enables sustained flows, *Nature Communications* **16**, 530 (2025).
- [64] D. M. Sussman, cellgpu: Massively parallel simulations of dynamic vertex models, *Computer Physics Communications* **219**, 400 (2017).
- [65] C. W. Chan, D. Wu, K. Qiao, K. L. Fong, Z. Yang, Y. Han, and R. Zhang, Chiral active particles are sensitive reporters to environmental geometry, *Nature Communications* **15**, 1406 (2024).
- [66] A. Fletcher, M. Osterfield, R. Baker, and S. Shvartsman, Vertex models of epithelial morphogenesis, *Biophysical Journal* **106**, 2291 (2014).
- [67] L. Puggioni, D. Krommydas, and L. Giomi, Collective migration and topological phase transitions in confluent epithelia, *arXiv [cond-mat.soft]* (2025).
- [68] D. L. Weaire and S. Hutzler, *The Physics of Foams* (Oxford University Press, New York, 1999).
- [69] H. Ren, W. Wang, W. Tang, and R. Zhang, Machine eye for defects: Machine learning-based solution to identify and characterize topological defects in textured images of nematic materials, *Physical Review Research* **6**, 013259 (2024).
- [70] F. Pérez-Verdugo and S. Banerjee, Tension remodeling regu-

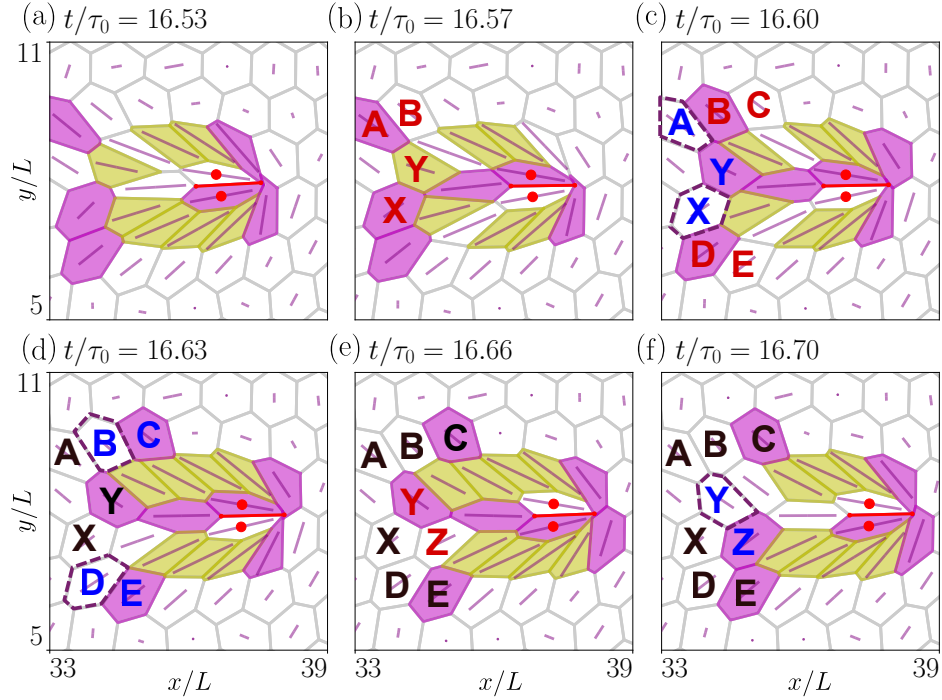


FIG. 20. Snapshots of the auto-healing packet, the dot lines highlight the healing  $+L$  defects in the previous snapshot. The cell markers in red represent the changing of neighbors in the next frame while markers in blue indicate the change is made from last frame. (a–f) Snapshots captured at the instant of T1 transition initiation in the back region of the forwarding packet.

- lates topological transitions in epithelial tissues, *PRX Life* **1**, 023006 (2023).
- [71] A. Pasupalak, L. Yan-Wei, R. Ni, and M. Pica Ciamarra, Hexatic phase in a model of active biological tissues, *Soft Matter* **16**, 3914 (2020).
- [72] R.-x. Guo, J.-j. Li, and B.-q. Ai, Melting of two-dimensional deformable particle systems, *Physica A: Statistical Mechanics and its Applications* **623**, 128833 (2023).
- [73] D. T. Tambe, C. Corey Hardin, T. E. Angelini, K. Rajendran, C. Y. Park, X. Serra-Picamal, E. H. Zhou, M. H. Zaman, J. P. Butler, D. A. Weitz, J. J. Fredberg, and X. Trepate, Collective cell guidance by cooperative intercellular forces, *Nature Materials* **10**, 469 (2011).
- [74] X. Trepate and J. J. Fredberg, Plithotaxis and emergent dynamics in collective cellular migration, *Trends in Cell Biology* **21**, 638 (2011).
- [75] J.-M. Armengol-Collado, L. N. Carenza, J. Eckert, D. Krommydas, and L. Giomi, Epithelia are multiscale active liquid crystals, *Nature Physics* 10.1038/s41567-023-02179-0 (2023).
- [76] L. Mohan, M. Cloitre, and R. T. Bonnecaze, Active microrheology of soft particle glasses, *Journal of Rheology* **58**, 1465 (2014).
- [77] A. Hopkins, M. Chiang, B. Loewe, D. Marenduzzo, and M. C. Marchetti, Local yield and compliance in active cell monolayers, *Physical Review Letters* **129**, 148101 (2022).
- [78] P. Martin and S. M. Parkhurst, Parallels between tissue repair and embryo morphogenesis, *Development* **131**, 3021 (2004).
- [79] V. Lecaudey and D. Gilmour, Organizing moving groups during morphogenesis, *Current Opinion in Cell Biology* **18**, 102 (2006).
- [80] P. Friedl and K. Wolf, Tumour-cell invasion and migration: diversity and escape mechanisms, *Nature Reviews Cancer* **3**, 362 (2003).
- [81] T. Omelchenko, J. M. Vasiliev, I. M. Gelfand, H. H. Feder, and E. M. Bonder, Rho-dependent formation of epithelial “leader” cells during wound healing, *Proceedings of the National Academy of Sciences* **100**, 10788 (2003).
- [82] L. Qin, D. Yang, W. Yi, H. Cao, and G. Xiao, Roles of leader and follower cells in collective cell migration, *Molecular Biology of the Cell* **32**, 1267 (2021).
- [83] X. Tang and J. V. Selinger, Orientation of topological defects in 2d nematic liquid crystals, *Soft Matter* **13**, 5481 (2017).

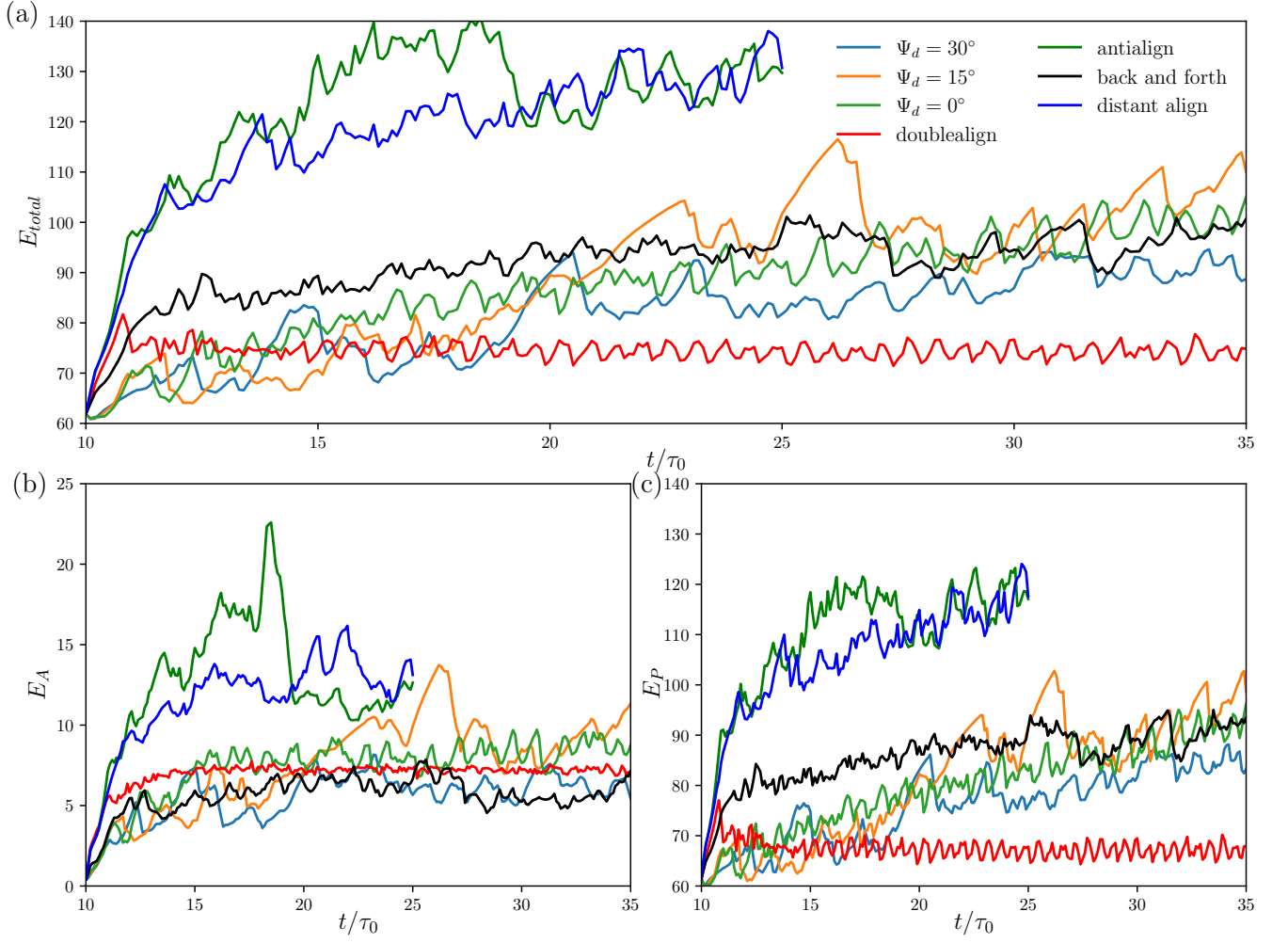


FIG. 21. (a) Free energy  $E_{total} = E_{AVM'}$  and corresponding energy terms (b)  $E_A$  and (c)  $E_P$  as a function of time in the single-cell drag simulation at  $\Psi_d = 0^\circ, 15^\circ, 30^\circ$ , and in the double-cell drag simulation as indicated in the legend. The energy is evaluated at  $\bar{v}_0 = 0.1$  and  $p_0 = 3.65$ .

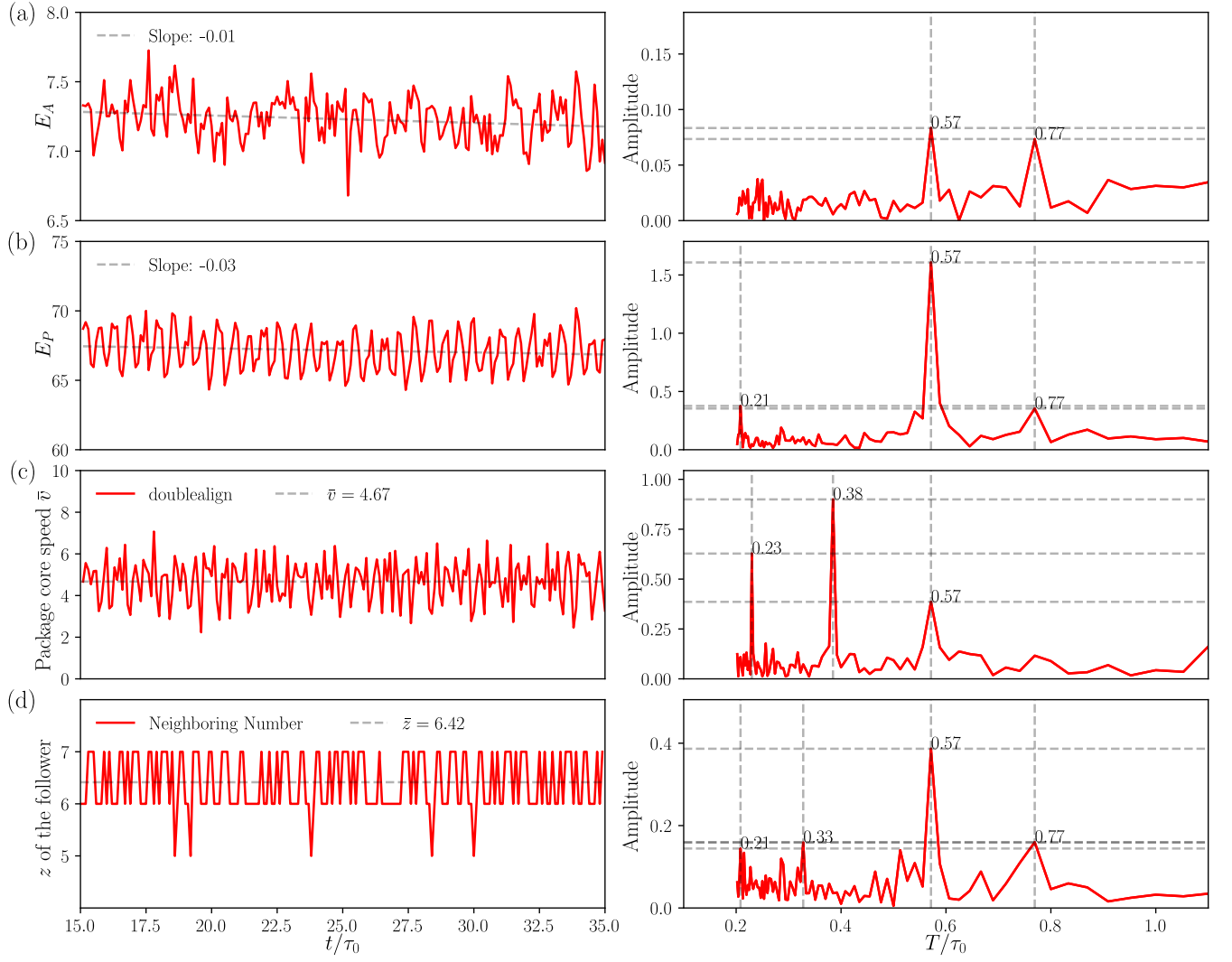


FIG. 22. Temporal behavior (left column) and the corresponding spectrum (right column) in the period domain (inverse frequency space) of the cell's energy term (a)  $E_A$ , (b)  $E_P$ , (c) packet core speed  $\bar{v}$ , and (d) coordination number  $z$ .

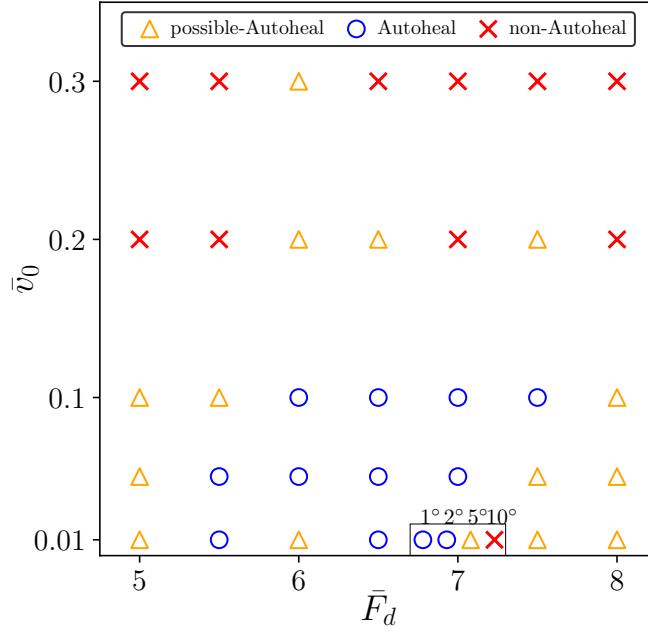


FIG. 23. The phase diagram of the auto-healing configuration for various values of  $\bar{v}_0$  and  $\bar{F}_d$  at  $p_0 = 3.65$  and  $\Psi_d = 0^\circ$ . Additional angle variance is introduced at  $\bar{v}_0 = 0.01$  and  $\bar{F}_d = 7$ .

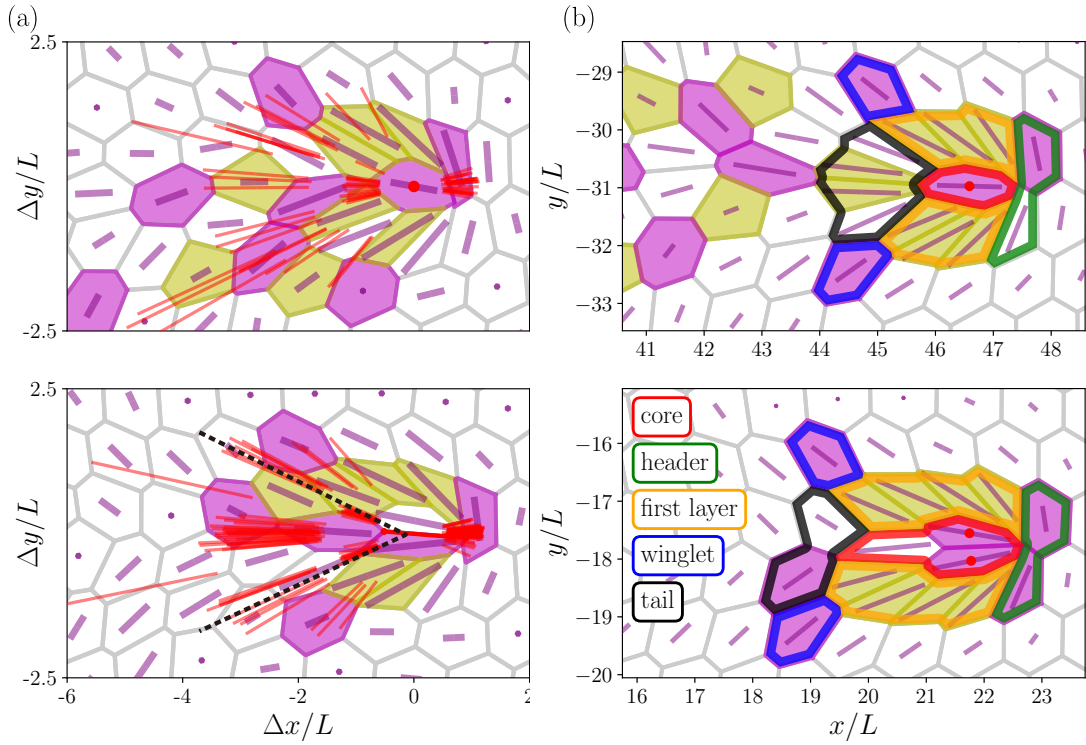


FIG. 24. Comparison of (a) the T1 transition heatmap and (b) cell roles between single-drag and double-drag configurations at  $\Psi_d = 0^\circ$ . Red bars indicate T1 transition events in the direction of losing neighbors.